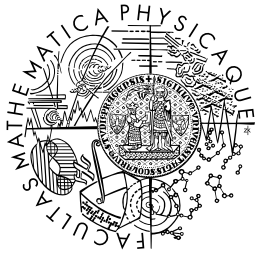

FACULTY
OF MATHEMATICS
AND PHYSICS
Charles University

BACHELOR THESIS

Kryštof Jasenský

Terahertz spectroscopy of altermagnets

Department of Chemical Physics and Optics

Supervisor of the bachelor thesis: RNDr. Lukáš Nádvorník, Ph.D.
Study programme: Physics
Study branch: Physics

Prague 2023

I declare that I carried out this bachelor thesis independently, and only with the cited sources, literature and other professional sources. It has not been used to obtain another or the same degree.

I understand that my work relates to the rights and obligations under the Act No. 121/2000 Sb., the Copyright Act, as amended, in particular the fact that the Charles University has the right to conclude a license agreement on the use of this work as a school work pursuant to Section 60 subsection 1 of the Copyright Act.

In ..... date ....

Author's signature

Firstly, I would like to thank my supervisor Lukáš Nádvorník for introducing me to the field of spintronics and allowing me to participate in research in this field. His passion for science and exceptional ability to promote it are truly admirable and I do believe this has furthered my own dedication to work on the thesis. Furthermore, I wish to thank him for all the guidance he has given me and the answers to my numerous questions, delivered with unprecedented clarity.

Secondly, I would like to thank my lab partner, Jiří Jechumtál, as the work would not be possible without him. Our cooperation was seamless, the conversations enriching and entertaining, and he answered every research topic-related question as well as he could.

I also wish to acknowledge the help of Kamil Olejník, who operated magnetometric instruments, discussed measurement results with us and helped me with magnetometric measurements data processing. Likewise, this thesis would not be possible without the manufacturers of our samples, Gabriele de Luca and Daniel Scheffler.

Moreover, I would like to thank my friends and family, especially those without any physics background, for being unafraid to ask that I explain my research efforts to them. Providing them with somewhat coherent and understandable explanations required a thorough understanding of the subject-matter and many of these conversations helped me discover where my own knowledge was lacking, forcing me to delve deeper into the theory.

Lastly, I wish to acknowledge my high school informatics teacher, Jana Kašpárková, who taught me how to work with a vector graphics editor. A skill which has been surprisingly useful throughout my studies, as is hopefully demonstrated by the illustrations I created for this thesis.

Title: Terahertz spectroscopy of altermagnets

Author: Kryštof Jasenský

Department: Department of Chemical Physics and Optics

Supervisor: RNDr. Lukáš Nádvorník, Ph.D., Department of Chemical Physics and Optics

Abstract: Recent advances in theoretical understanding of magnetic solids have shown that by utilising a more general spin-symmetry description and defining a new elementary magnetic phase—altermagnetism, in addition to ferromagnetism and antiferromagnetism, we may interpret certain properties of magnetic materials which did not match the ferromagnetic nor the antiferromagnetic description. Properties of altermagnets have been predicted, and some have been experimentally confirmed in certain materials. The thesis focuses on an altermagnetic material, ruthenium dioxide (RuO_2). The aim is to explore its altermagnetic properties and generation of spin currents in the material by means of terahertz spectroscopy. For this purpose, nine bilayers with metal, ferromagnetic and RuO_2 layers were manufactured. The bilayers were excited with femtosecond pulses from a titanium-sapphire laser to generate THz waves, and the radiation was detected by the standard THz time-domain spectroscopy method. Terahertz emission from bilayers with RuO_2 was found to be low, as compared to standard spintronic THz emitters, although observable. Possible explanations of the signal magnitude are given in the discussion. The detected signals were dependent on the crystal orientation; however, their microscopic sources remain unclear.

Keywords: spintronics, altermagnets, terahertz spectroscopy, ruthenium dioxide

Contents

Introduction **2**

1 Theory **3**
1.1 Spin . . . 3
1.2 Spin-orbit interaction . . . 3
1.3 Spin current . . . 4
1.4 Spin Hall effects . . . 5
1.5 Collinear magnetism . . . 6
1.6 Magnetic hysteresis and exchange bias . . . 7
1.7 Altermagnetism . . . 8

2 Experimental methods **11**
2.1 Spintronic terahertz emitters . . . 11
2.2 Generating THz pulses with RuO2 bilayers . . . 13
2.3 Terahertz spectroscopy . . . 16
2.4 Laboratory setup for THz wave generation and detection . . . 17
2.5 Sample growth . . . 19
2.6 Sample multilayers . . . 20
2.7 Superconducting quantum interference device (SQUID) . . . 22

3 Measurement results **23**
3.1 SQUID measurements . . . 23
3.2 CoFeB/Pt reference sample . . . 26
3.3 RuO2 samples with CoFeB layer . . . 27
3.3.1 Samples ln10e and ln10h . . . 28
3.3.2 Sample ln10b . . . 30
3.3.3 Magnetic and nonmagnetic signals . . . 31
3.4 RuO2 samples with Pt layer . . . 33

4 Summary and discussion **36**
4.1 RuO2 samples with CoFeB layer . . . 36
4.2 RuO2 samples with Pt layer . . . 39
4.3 Future experiments . . . 40

Conclusion **41**

Bibliography **42**

List of Figures **46**

Introduction

This thesis deals with magnetic materials called altermagnets. Altermagnets are magnetic materials with distinct properties previously related to either ferromagnets or antiferromagnets. Altermagnets have zero net magnetisation and thus no external magnetic field because magnetic moments of neighbouring atoms or molecules are oriented opposite and cancel each other out. This is a fundamental characteristic of antiferromagnets. However, altermagnets have anisotropically spin-split electron energy bands which are more akin to ferromagnetic materials [1].

We study altermagnets in the context of spintronics. It is a field of electronics in which mechanisms regarding spin and its transport are studied and used in spintronic devices [2]. Spintronic devices usually utilise a magnetic material for spin current generation or detection, therefore, it is of high importance for spintronics to find magnetic materials most suitable for its applications.

Magnetic materials most commonly used in contemporary spintronic devices, such as memory bits or reading heads in hard drives, are ferromagnets whose properties are well understood. However, the use of ferromagnets has its disadvantages. As ferromagnets have non-zero net magnetisation, the generated demagnetising magnetic field (stray field) might change the magnetisation of other ferromagnetic materials in the vicinity (and vice-versa may itself be changed by the fields generated by these). This limitation imposed on the scaling of magnetic devices vanishes with the use of antiferromagnets in place of ferromagnets because antiferromagnets do not generate stray magnetic fields [3]. And generally, to change the magnetic structure of an antiferromagnet, a much stronger magnetic field needs to be applied than in the case of changing the magnetic structure of a ferromagnet. Another important and perspective aspect of antiferromagnets is that their magnetic structure dynamics are expected to be much faster than those of ferromagnets, reaching picosecond time scales. This might prove especially useful in antiferromagnetic memories, which could theoretically operate at terahertz (THz) frequencies, a regime beyond the reach of their ferromagnetic counterparts.

To study the possible ultrafast spin current dynamics in altermagnets, spintronic THz emitters (STEs) can be utilised. These are magnetic-metal multi-layers that produce ultrashort pulses of THz radiation when excited with optical femtosecond laser pulses. STEs are relatively low-cost sources of THz radiation with larger, gapless bandwidth than other affordable sources [4]. In short, STEs work in a manner that a spin current is generated across the layers by the optical excitation and then it is converted to an electric current generating the THz pulse. STEs are not only efficient sources of THz radiation, but the principle of STEs can be exploited to study spin currents and resulting electric currents in materials by detecting the THz pulse.

Recent papers have shown that the low-frequency (GHz and lower) conversion of spin current into an electric current occurs in RuO_2 (now considered altermagnetic [1]) and others have experimentally measured the ratio of spin current to resulting charge current [5, 6]. We aim to explore their ultrafast analogues by means of THz spectroscopy.

1. Theory

1.1 Spin

Spin is a quantity carried by elementary particles and it is a type of angular momentum in quantum mechanics. Unlike orbital angular momentum, spin is an intrinsic property of particles and does not directly depend on the motion state of the particle. Its existence was first postulated by Uhlenbeck and Gouldsmith for the interpretation of atomic spectra, and later, Paul Dirac showed that by merging the theory of special relativity and quantum mechanics, spin naturally arises from the relativistic equivalent of Shrödinger equation called Dirac equation [7].

Angular momenta in quantum mechanics are quantised and have discrete spectra. They are defined by their commutation relations:

$$[J_i, J_j] = i\hbar\varepsilon_{ijk}J_k \tag{1.1}$$

$$\left[J_i, \boldsymbol{J}^2\right] = 0 \tag{1.2}$$

where $\boldsymbol{J}$ denotes the quantum angular momentum vector operator, J_i its components and $\boldsymbol{J}^2 = \sum_i J_i J_i$ its norm squared. The same commutation relations remain valid for spin angular momentum vector operator $\boldsymbol{S}$. Analogously to classical mechanics, angular momenta and spin of charged particles are connected with the magnetic moment of the particles:

$$\boldsymbol{\mu}_L = \frac{-e}{2m}\boldsymbol{L}, \text{ respectively } \boldsymbol{\mu}_S = -g_0\frac{e}{2m}\boldsymbol{S} \tag{1.3}$$

in which e denotes the charge of the particle, m its mass, $\boldsymbol{\mu}$ magnetic moments resulting from angular momentum and spin and g_0 denotes the g-factor which is approximately 2 for free electrons [8].

Electrons are charged elementary particles and have a spin of magnitude $1/2$ (in SI units $\hbar/2$, $\hbar$ being the reduced Planck constant) and two possible projections[1] of spin: $1/2$ and $-1/2$ (commonly called spin *up* or *down*).

1.2 Spin-orbit interaction

Briefly, we shall introduce the spin-orbit interaction, also called spin-orbit *coupling*. This interaction is of a relativistic origin and can be formally derived from the aforementioned Dirac equation. It is the interaction between particle spin and its (orbital) momentum that occurs when a particle moves in a potential.

To get an intuitive grasp of this interaction, we might imagine a particle moving through a static electric field from the laboratory frame of reference. Suppose we calculate the electromagnetic field from the particle's frame of

[1] As components of the spin operator do not commute, only one component of spin can be measured because of uncertainty relations. When considering spin in spintronics, the projection into the axis parallel to magnetisation or intensity of the magnetic field is often the chosen component.

reference (where the particle is stationary) by the Lorentz transformation. In that case, we find that a magnetic field resulting from the transformation of the electric field exists in this frame of reference [9]. Thus, we might think of the spin-orbit interaction as the Zeeman interaction between the spin magnetic moment of the particle and the effective magnetic field in the particle frame of reference. Let us note that this approach would give us the spin-orbit interaction term in energy too large by the factor of 2.

1.3 Spin current

As in the case of flow of charge represented by an electric current density $\boldsymbol{j}_c$, we describe the transport of spin angular momentum by a spin current density[2] $\boldsymbol{j}_s$. The ideologically simplest form of spin current occurs in a flow of electrons (or, more generally, charge carriers) when there is a difference between the flow of electrons with spin up and electrons with spin down [7]. Let us denote the current carried by electrons with spin up by $\boldsymbol{j}_\uparrow$ and the current carried by electrons with spin down by $\boldsymbol{j}_\downarrow$. Then the total electric current $\boldsymbol{j}_c$ is:

$$\boldsymbol{j}_c = \boldsymbol{j}_\uparrow + \boldsymbol{j}_\downarrow \tag{1.4}$$

If we imagine the two currents $\boldsymbol{j}_\uparrow$ and $\boldsymbol{j}_\downarrow$ as carrying the spins in the direction of electron flow for each spin projection, we easily come to the value of spin current carrying up spin:

$$\boldsymbol{j}_s = \boldsymbol{j}_\uparrow - \boldsymbol{j}_\downarrow \tag{1.5}$$

This kind of spin current is called *conduction-electron spin current*. We shall call an electric current spin polarised if, in addition to the electric current, there is also a parallel net spin current carried by it.

However, unlike charge, spin-polarisation (preferred collective orientation of spin in one direction) is not conserved and the spin current is dissipated after a certain distance travelled in a material. If spin-polarisation were a conserved quantity, we might define the conduction-electron spin current in terms of the continuity equation [10]:

$$\frac{\partial}{\partial t}\boldsymbol{M}(\boldsymbol{r},t) = -g_e \,\mathrm{div}\boldsymbol{j}_s(\boldsymbol{r},t), \tag{1.6}$$

where $\boldsymbol{r}$ stands for spatial coordinates, t for time and $\boldsymbol{M}$ is the local magnetisation (magnetic moment density). This equation represents the idea that electrons carry magnetic moment, which is directly tied to their spin and thus, factor g_e is the g-factor for electrons. We can add a term $\boldsymbol{T}$ accounting for nonconservation of spin to the continuity equation (1.6):

$$\frac{\partial}{\partial t}\boldsymbol{M}(\boldsymbol{r},t) = -g_e \,\mathrm{div}\boldsymbol{j}_s(\boldsymbol{r},t) + \boldsymbol{T} \tag{1.7}$$

The added term $\boldsymbol{T}$ represents the generation and relaxation of spin current. Usually, this term is treated phenomenologically and the simplest

[2]We will drop the word density for brevity. We will always assume that we mean the current density when writing equations. The general ideas apply to both.

phenomenological model of $\boldsymbol{T}$ is the *single pole model* [7]:

$$\boldsymbol{T} = -\frac{\boldsymbol{M} - \boldsymbol{M}_0}{\tau}, \tag{1.8}$$

where $\boldsymbol{M}_0$ is the equilibrium magnetisation and τ is the spin relaxation time constant—the time after which the deviation from equilibrium magnetisation lowers to a certain fraction of its initial value. This constant can be approximated by different models of spin current relaxation in materials [2, 11].

Let us mention two major mechanisms of spin relaxation for the conduction-electron spin current. The first is the D'yakonov and Perel mechanism in which the spin current relaxes due to the fact that the spin-orbit interaction causes conduction electrons' spin to precess around random effective magnetic fields caused by the spin-orbit interaction. Because conduction electrons follow different paths in a material, their spins precess differently and the spin polarisation of a current is progressively lost. The second is the Elliot-Yafet mechanism where the spin-orbit interaction can cause the spin of an electron to *flip* (change signs) when scattered.

There are different forms of spin-currents other than conduction electrons such as magnons (spin-waves) [10, 7]. Generally, spin current need not be connected with the transport of its carriers at all. However, the conduction electron spin current will be the most important for our case.

1.4 Spin Hall effects

Spin Hall effects are processes where an electric current in a non-magnetic metal causes a spin current perpendicular to the plane defined by the electric current and spin angular momentum direction of the charge carriers [12]. This is, of course, strongly analogous to the Hall effect where voltage arises between the two edges of a material perpendicular to the magnetic field applied and the electric current flowing through the material because Lorentz force curves the charges' trajectories [8].

In the case of the spin Hall effect, its source is the spin-orbit interaction. The physical principles of the spin-orbit interaction giving rise to the spin Hall effect are quite rich and complex and it is experimentally challenging to distinguish the microscopic mechanism responsible for the observed spin Hall effect [12]. The first explanations of the spin Hall effect linked the spin current to the scattering of flowing electrons on impurities in the crystal lattice which is spin-dependent due to the spin-orbit coupling. Later approaches showed that the spin Hall effect might occur even in the absence of impurities because the periodic potential of crystal lattice gives rise to effective magnetic fields [7, 12]. Spin Hall effects caused by the effects related to the spin-orbit interaction of conduction electrons in the potential of lattice impurities are called *extrinsic* whereas spin Hall effects related to spin-orbit interaction of conduction electrons in the periodic lattice potential are called *intrinsic*.

Without considering the microscopic origin, we might describe the spin Hall effect for electric current $\boldsymbol{j}_c$, up spin direction $\boldsymbol{e}_s$ (which is a unit vector), by an equation:

$$\boldsymbol{j}_s^{\mathrm{SH}} = \gamma_{\mathrm{SH}}(\boldsymbol{e}_s \times \boldsymbol{j}_c), \tag{1.9}$$

where γ_{SH} is called *spin Hall angle* and it is the measure of how efficient the generation of transversal spin current $\boldsymbol{j}_s^{\mathrm{SH}}$ from longitudal electric current $\boldsymbol{j}_c$ is. There exists another effect called the inverse spin Hall effect which shares the same mechanisms. The difference is that in the inverse spin Hall effect, the electric current $\boldsymbol{j}_c^{\mathrm{SH}}$ arises from the flow of spin current $\boldsymbol{j}_s$ and we might write:

$$\boldsymbol{j}_c^{\mathrm{SH}} = \gamma_{\mathrm{SH}}(\boldsymbol{e}_s \times \boldsymbol{j}_s) \tag{1.10}$$

Both effects are visualised in Fig. 1.1. The spin Hall angle depends on the material.

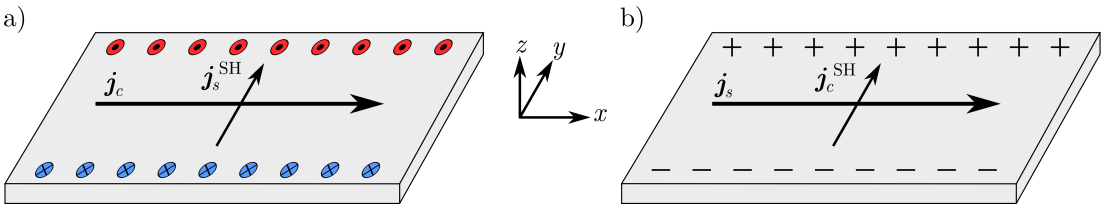

Figure 1.1: Schematical illustration of spin Hall effects. a) Electric current $\boldsymbol{j}_c$ along x-axis causes perpendicular spin current $\boldsymbol{j}_s^{\mathrm{SH}}$ along y-axis with spin direction along z-axis. Electrons with opposite spins gather at the edges. b) Spin current $\boldsymbol{j}_x$ along x-axis causes perpendicular electric current $\boldsymbol{j}_c^{\mathrm{SH}}$ along y-axis. The opposite charge accumulates at the edges.

1.5 Collinear magnetism

Magnetic fields are usually generated by electric current or by the magnetisation of materials. The sources of such magnetisation are individual dipole magnetic moments of constituent atoms and conduction electrons. In atoms, the magnetic moment is the result of orbital angular momentum and spin of electrons (nuclei possess magnetic moments too, but these are three orders of magnitude smaller than those of the electrons [8]). In solids, the magnetism related to magnetic moments generated by spin is much stronger [13]. In this section, we will describe a collinear form of magnetism in solids – collinear meaning that the magnetic momenta of magnetic atoms in the crystal lattice are either parallel or antiparallel.

Ferromagnets (ferromagnetic materials) are solids in which atoms with non-zero magnetic moments spontaneously align in the same direction, producing a net magnetisation. This behaviour is due to interactions between electrons of neighbouring atoms in the material and is highly dependent on the chemical and crystal structure. The basic description of interatomic interactions leading to ferromagnetic phase is the description by *exchange* interactions which describe the effect of electrostatic repulsion of electrons and the effect of Pauli exclusion principle[3]. Mathematically we express the exchange interaction of one atom (denoted by i) by the following Hamiltonian [8]:

$$\boldsymbol{H}_i = -2\sum_{i \neq j} \mathcal{J}_{ij}(\boldsymbol{R}_{ij})\boldsymbol{S}_i \cdot \boldsymbol{S}_j, \tag{1.11}$$

[3]A principle which states that, in quantum mechanics, two identical particles with half-integer spin cannot occupy the same quantum one-particle state.

where we sum over the total spin of other atoms $\boldsymbol{S}_j$, $\boldsymbol{S}_i$ is the spin of the atom and $\mathcal{J}_{ij}$ is the exchange constant, a scalar function of relative position $\boldsymbol{R}_{ij}$ between the atoms (typically, $\mathcal{J}_{ij}$ is independent of the direction of $\boldsymbol{R}_{ij}$ [13]). The sum can be simplified by summing over just a few neighbouring atoms and by setting $\mathcal{J}_{ij}$ constant and independent of $\boldsymbol{R}_{ij}$. Then we can arrive at the conclusion that if $\mathcal{J} > 0$, ferromagnetic order is favourable. We observe the ferromagnetic order in substances at temperatures lower than the Curie temperature T_C, which is specific for each material. When the temperature is higher than T_C, thermal fluctuations are so strong that the ferromagnetic order is lost[4].

In antiferromagnets, the interactions between neighbouring atoms favour antiparallel orientation of magnetic moments which would correspond to $\mathcal{J} < 0$ in formula (1.11). In the crystal lattice, we identify two sublattices with opposite magnetic moments [14]. A temperature at which the magnetic order is lost is called Néel temperature T_N.

Another type of collinear magnetism is ferrimagnetism where the magnetic moments of some atoms in the solid are non-zero and antiparallel. However, the magnitude of opposite magnetic moments is not equal so a net magnetisation of the material is present the same as in ferromagnets [14].

1.6 Magnetic hysteresis and exchange bias

Magnetic hysteresis is a phenomenon present in (for example) ferromagnetic materials where the magnetisation depends on previously applied magnetic field. Generally, the atoms tend to react to the external magnetic field in some manner but regarding hysteretic effects, the magnetic structure is different after the material is put in and out of a magnetic field than it was before [8]. Hysteresis is typically shown as hysteresis loops which are graphs of material magnetisation M (or magnetic induction B or magnetic moment m) plotted against an external applied field H, see Fig. 1.2. In ferromagnets (in the ferromagnetic phase), hysteresis is present as a result of the behaviour of microscopic magnetic *domains*. These are parts of the material where singular atomic magnetic moments align in one direction. The domains might not be oriented all in parallel and with a sufficient magnetic field, we can *saturate* the ferromagnet, meaning the domains align in one direction, the direction of the field. This orientation mostly remains after the field is no longer present [8].

The behaviour of magnetic materials differs in the bulk of the material and on the surface. It may differ substantially because magnetic material phenomena are very closely tied to interactions of neighbouring atoms. When antiferromagnetic and ferromagnetic thin films are in contact, an effect called *exchange bias* may occur. The exchange interaction between atoms in ferromagnetic and antiferromagnetic layers causes additional anisotropy. Such anisotropy is then manifested as a shift of the origin of the hysteresis loop in a hysteretic diagram (magnetisation of the bilayer is mostly produced by the ferromagnetic layer), see Fig. 1.2. This occurs when the Curie temperature of the ferromagnetic layer exceeds the Néel temperature of the antiferromagnetic layer. Exchange bias

[4]We say that the material is in the *ferromagnetic phase* and, in fact, we might describe the process where material loses magnetic properties at T_C as a phase transition [8].

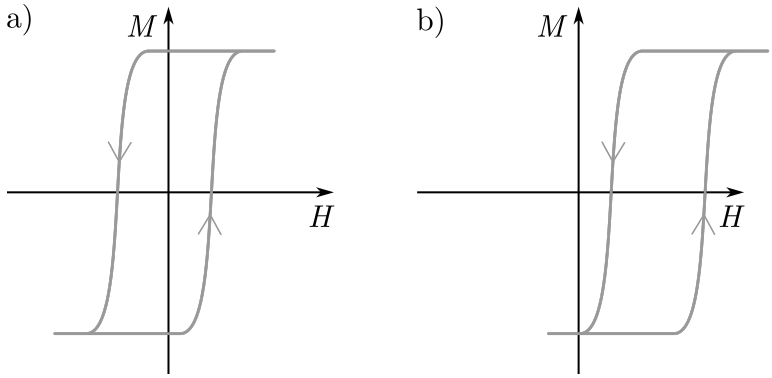

Figure 1.2: Illustrative dependence of material magnetisation M on applied magnetic field H (in the easy axis direction[5]). a) A hysteresis loop of a ferromagnet. Once the material is magnetically saturated, the magnetisation stops increasing with the rising magnetic field. Non-zero magnetisation remains in a zero field. Arrows on the curves indicate magnetisation for decreasing and increasing fields. b) Magnetisation dependence of a ferromagnet-antiferromagnet bilayer. Due to exchange bias, the hysteresis loop is not centred around the zero field.

is dependent on the atomic structure of the interface. To achieve observable exchange bias, the bilayer is heated above the Néel temperature and then cooled with an applied field sufficient enough to align the domains in the ferromagnetic layer (this process is called *field cooling*) [8].

1.7 Altermagnetism

In the previous section, we briefly described two types of conventionally recognised magnetic phases with collinear-compensated magnetic order (ferromagnetic and antiferromagnetic) and their microscopic origin. Recent theoretical predictions define another distinct magnetic phase of collinear magnetic materials dubbed *altermagnetic* (the phenomena—altermagnetism) [1]. In this magnetic phase, the magnetic moments of two sublattices are compensated like in antiferromagnets. However, altermagnetic materials can possess, due to their specific magnetic and crystalline symmetries, anisotropically spin-split band structure (see Figures 1.3, 1.4), absent in antiferromagnets and typical for ferromagnets. Experimental findings of predicted phenomena unparalleled in either ferromagnets or antiferromagnets supported the theoretical expectation [5, 15]s. In recent works, articles [1] and [16], a symmetry description approach has been proposed which uses non-relativistic spin-space combined with real-space symmetry description. Based on symmetries in magnetic materials, three distinct phases are recognised: ferromagnetic, antiferromagnetic and altermagnetic. Now, we illustrate how altermagnets differ from antiferromagnets from the symmetry perspective. In a collinear antiferromagnet, two sublattices with magnetic atoms are connected by the change of spin from up to down (time inversion) and translation of the atoms in the real space (by one sublattice

[5]Easy axis direction is a direction in which the magnetisation of magnetic material is energetically most favourable.

constant) as in antiferromagnets. In contrast, the sublattices in altermagnets are connected by a change of spin and rotation combined with a translation of the atoms in real space. This is illustrated in Figure 1.3.

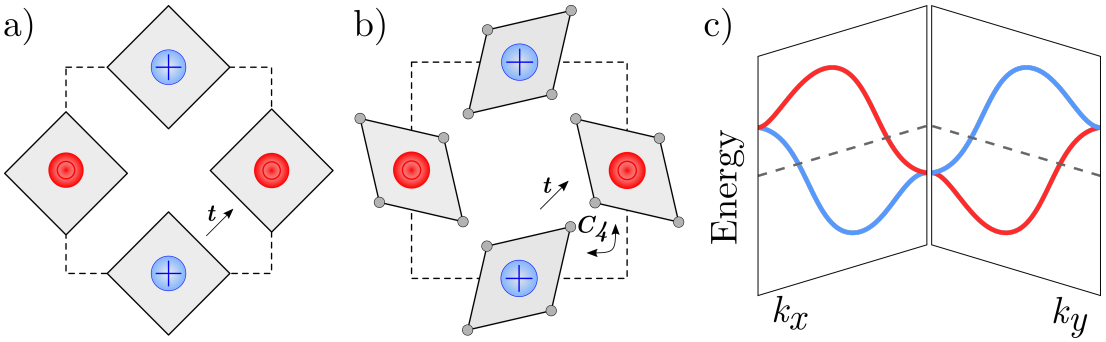

Figure 1.3: a) The illustration of symmetry relations of antiferromagnet sublattices. Red circles symbolise atoms with spin up and blue circles spin-down atoms. The sublattices with opposite magnetic moments are connected by the real-space translation $\boldsymbol{t}$ and spin-reversal operations. b) The illustration of symmetry relations of altermagnetic sublattices. The sublattices with opposite magnetic moments are connected by the real-space translation $\boldsymbol{t}$, rotation $\boldsymbol{C}$ (in this case four-fold) and spin-reversal operations. c) The spin-split anisotropic band structure present in altermagnets. Red curves represent the spin-up electron energetic band and blue curves represent the spin-down electron band, k stands for the wave vector of electrons.

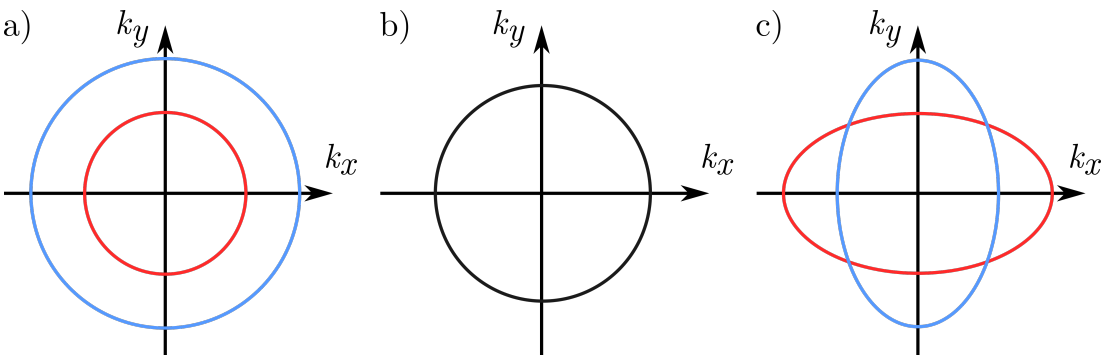

Figure 1.4: Schematic illustration of spin-resolved Fermi surfaces in 2D wavevector space. Red curves represent spin-up electrons and blue spin-down electrons. a) Ferromagnet. The structure is spin-dependent but isotropic. b) Antiferromagnet. The structure is independent of spin (it is spin-degenerated, hence the black colour). c) Altermagnet. The structure is spin-dependent and anisotropic.

Altermagnetic materials are promising systems for spintronic applications for several reasons. (i) The zero net magnetisation means that there is no stray field outside the altermagnet which allows for higher bit integration in magnetic memories. (ii) The spin order dynamics in altermagnets is on the close-to-picosecond timescale, like in antiferromagnets [1], which is promising for an ultra-fast operation of magnetic memories. (iii) The spintronic phenomena in altermagnets are of non-relativistic origin as opposed to the effects exploited in antiferromagnetic materials, which are based on relativistic spin-orbit coupling. The non-relativistic altermagnetic effects are scaling with the exchange interaction, therefore, are expected to be orders of magnitude larger than the relativistic ones. (iv) Another notable prediction of ref. [1] is the relative abundance of altermagnetic materials in nature. In fact, almost a third of 32 Laue crystallographic groups with equal collinear-compensated spin arrangements (i.e. ferromagnetic, antiferromagnetic or altermagnetic phase is possible) contain symmetries specific for the altermagnetic phase [16].

2. Experimental methods

2.1 Spintronic terahertz emitters

Spintronic THz emitters (shortly STEs) are nanometer-thin multilayers, usually bilayers, of ferromagnetic (FM) and nonmagnetic (NM) metals which emit substantial THz radiation when irradiated by femtosecond laser pulses [4]. The physical principle is based on the generation of spin-polarised flowing current flowing from the ferromagnetic to the nonmagnetic layer which is then converted into a transversal ultrafast current in the NM layer where it generates a THz electromagnetic wave.

First, the femtosecond laser *pump* pulse excites electrons in FM and NM layers to non-equilibrium states. Because the transport properties in the FM layer differ for charge carriers with majority spin orientation and for charge carriers with minority spin orientation, the spin current begins to flow into the NM layer [17]. Here, a transverse charge current is produced by an effect that asymmetrically scatters electrons with spin up and spin down; in common STEs, it originates from the inverse spin Hall effect (ISHE). The relaxation towards equilibrium happens on a timescale of hundreds of femtoseconds [18]. The dynamic generation and relaxation of charge current in the NM layer acts as a Hertzian dipole and a THz pulse is emitted. The emitted electromagnetic wave is linearly polarised. The process is illustrated in Fig. 2.1.

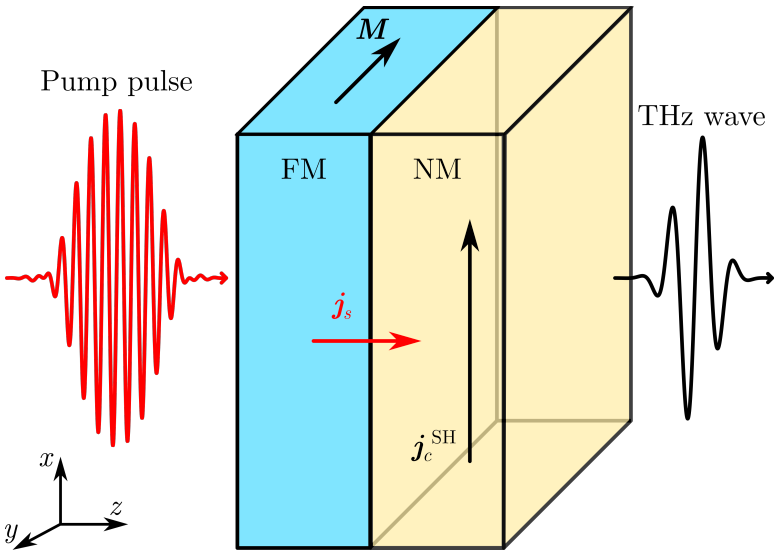

Figure 2.1: Ilustration of the principle of spintronic THz emission from ferromagnetic metal (FM) and nonmagnetic metal (NM) thin bilayer by fs laser pulse. First, the incident fs laser pulse excites charge carriers in the bilayer. Because of different carrier transport properties and densities for carriers with majority spin (the spin is in the direction of the FM magnetisation $\boldsymbol{M}$) in the FM layer, a spin current $\boldsymbol{j}_s$ is launched into the NM layer along the axis perpendicular to layer interface. The spin current $\boldsymbol{j}_s$ in the NM layer results in charge current $\boldsymbol{j}_c^{\mathrm{SH}}$ because of the ISHE. The generation and relaxation of charge current $\boldsymbol{j}_c^{\mathrm{SH}}$ is the source of the THz electromagnetic pulse.

The electric field of emitted wave in the frequency domain $E_{\mathrm{THz}}(\omega)$ directly behind the multilayer is given by generalised Ohm's law [4]:

$$E_{\mathrm{THz}}(\omega) = eZ(\omega) \int_{d_{\mathrm{FM}}}^{d} \gamma_{\mathrm{SH}} j_s(z,\omega) \mathrm{d}z, \tag{2.1}$$

where Z is the impendance of NM layer, j_s is the spin current in the NM layer, d is total thickness of the multilayer, d_{FM} is thickness of ferromagnetic layer[1], γ_{SH} is the spin Hall angle and e is the electron charge. This equation describes the generation of an electromagnetic wave by a charge current in the x-direction $j_c(z,\omega) = -e\gamma_{\mathrm{SH}}(z) j_s(z,\omega)$ resulting from the spin current j_s and ISHE. To express the relationship between material properties, laser beam energy and E_{THz}, we will make assumptions according to references [4] and [17]:

- The sample bilayer is so thin that we can approximate the outgoing wave as a plane wave and also that E_{THz} is constant in the bilayer at every moment.
- The majority-spin charge carriers which traverse the metal contribute to j_c in ISHE. The density of spin-polarised electrons decreases based on travelled distance s as $e^{-s/\lambda_{\mathrm{rel}}}$, where λ_{rel} is relaxation length in the NM metal.
- Spin carriers undergo total reflection at the interfaces of NM layer with FM layer and surrounding medium.
- Spin current generated by a pump laser pulse is proportional to its intensity[2] $I_{\mathrm{pump}} \propto |\boldsymbol{E}_{\mathrm{pump}}|^2$ and hence j_s is proportional to the fraction of absorbed energy from pump pulse inside the FM layer A_{FM} and $j_s \propto A_{\mathrm{FM}}$, where A is the absorbed energy.

Then we might estimate the amplitude of the electric field of the outgoing THz wave directly behind the NM layer in the case of ISHE by:

$$E_{\mathrm{THz}} \propto \gamma_{\mathrm{SH}} \lambda_{\mathrm{rel}} A_{\mathrm{FM}} \tanh\left(\frac{d_{\mathrm{NM}}}{2\lambda_{\mathrm{rel}}}\right) Z(\omega), \tag{2.2}$$

where d_{NM} is the thickness of NM layer.

An important advantage of using STEs over other sources of THz wave generation is the access to a large interval of THz frequencies while being relatively affordable [4]. The other exciting aspect of STEs lies in the novelty of the physical principles utilised. Studying the mechanisms in STEs means exploring the dynamics of electron transport in non-equilibrium systems with spin-dependent properties. By detecting and measuring the THz electric field $\boldsymbol{E}_{\mathrm{THz}}(\omega)$ of outgoing pulse, we can investigate the spin current $j_s(\omega)$.

[1] Thus we integrate in equation 2.1 over the thickness of the NM layer d_{NM}.

[2] This assumption is based on experimental results which suggest a linear relationship between pump pulse intensity I and E_{THz} amplitude [4].

2.2 Generating THz pulses with RuO_2 bilayers

RuO_2 has been considered a paramagnet until 2017 [19], when collinear antiparallel order was discovered. It has been classified as an antiferromagnet but in the classification scheme discussed in the section about altermagnets, RuO_2 is an example of altermagnetic material. It is a metal with a rutile crystalline structure belonging to the $P4_2/mnm$ space group. The Neél temperature of RuO_2 is above 375 K [20] so the magnetic order is not lost at room temperatures. In the crystalline structure, oxygen atoms form directional octahedrons around ruthenium atoms and in the sublattice, these octahedrons are rotated by 90°. The structure of RuO_2 crystal is shown in Fig. 2.2.

Theoretical predictions in [6] and experimental evidence in [5, 15] suggest that RuO_2 can be used to turn a spin-polarised electric current into a transversal charge current or to spin-polarise a longitudinal charge current. This is caused by the aforementioned anisotropic spin-split band structure in altermagnets with certain symmetry (so-called *d-wave*) and depends on the charge current orientation relative to the RuO_2 crystal orientation. The situation is schematically depicted in Fig. 2.3. In Fig. 2.4, we show how the electron energy Fermi surfaces change when an electric field is applied and thus (as RuO_2 is a semi-metal) current flows. In our bilayers, we generate the charge current by driving the electrons in the layers to excited states, resulting in them travelling between the layers. We are mainly interested in two situations: when charge current flows along $[0\bar{1}0]$ RuO_2 axis (then a *spin-splitter* effect occurs) and when current flows along $[1\bar{1}0]$ axis (then a *spin-polariser* effect occurs). The situations are visualised in Fig. 2.3.

If the charge current flows along $[0\bar{1}0]$ RuO_2 axis, the spin-split band structure causes spin-up and spin-down electrons to have different momenta (and velocities) along the perpendicular [100] axis. This creates a spin current perpendicular to spin orientation and the charge current direction. For THz waves to be emitted and subsequential detection of this process by THz spectroscopy, we polarise the charge current injected into the RuO_2 by a ferromagnetic layer in a similar manner as in STEs. For THz generation, we excite a ferromagnetic metal/RuO_2 bilayer by a laser pulse. The bilayer is manufactured in such a manner that the $[0\bar{1}0]$ direction in RuO_2 is perpendicular to the layer interface. Spin-polarised charge current from the ferromagnetic layer to RuO_2 is converted to transversal charge current in RuO_2 layer due to the spin-split band structure and the charge generates the THz wave.

If the charge current flows along $[1\bar{1}0]$ RuO_2 axis, spin up and spin down electrons have different momenta in the direction of current flow which results in the spin polarisation of the charge current. To generate THz radiation, we excite a nonmagnetic metal/RuO_2 bilayer. The crystallographic direction $[1\bar{1}0]$ in RuO_2 is perpendicular to the layer interface so a charge current from RuO_2 to the nonmagnetic layer is spin polarised. In the nonmagnetic layer, this current is converted via the inverse spin Hall effect to perpendicular charge current which emits the THz wave.

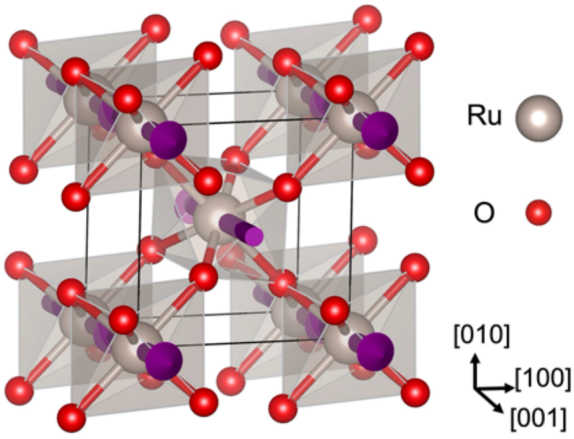

Figure 2.2: The structure of RuO_2 crystal. Purple arrows represent spins of Ru atoms (grey) which are surrounded by octahedrons formed by oxygen atoms (red). Crystallographic directions are shown in the bottom right corner. Taken from [5].

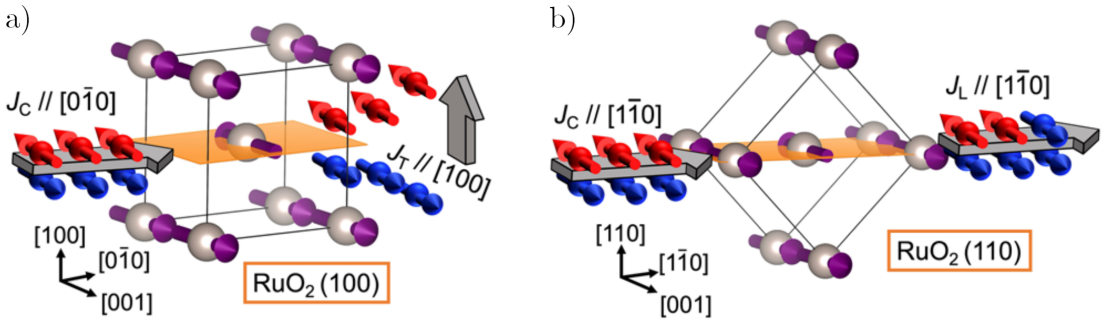

Figure 2.3: Illustration of spin currents resulting from spin-split band structure in RuO_2, blue and red spheres represent conduction electrons and grey spheres represent Ru atoms. Planes defined by charge current (J_C in the figure) and spin direction (red and blue coloured arrows for the conduction electrons and purple for Ru atoms) are indicated by Miller indices in parentheses. a) Charge current and spins define a (100) plane, the charge current flows along the [0$\bar{1}$0] axis and spin current (J_T, T for transverse) is generated in a direction perpendicular to the (100) plane. b) Charge current and spins define a (110) plane; the charge current flows along the [1$\bar{1}$0] direction and spin current (J_L, L for longitudinal) in the same direction is generated. Images taken from [5].

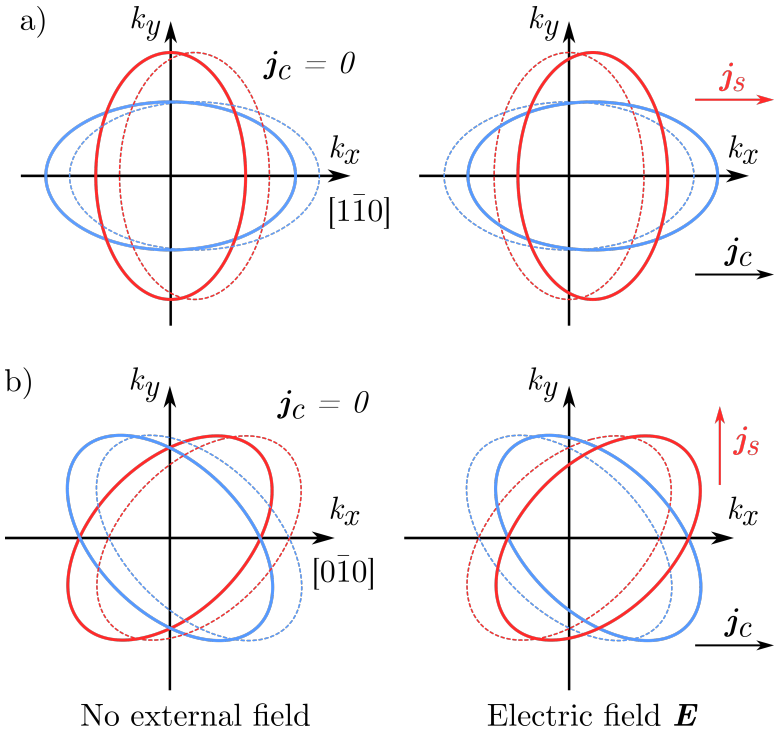

Figure 2.4: Schematic RuO_2 energy Fermi surfaces. When we apply an electric field $\boldsymbol{E}$ (in the figure, the applied electric field aims in the direction of the x-axis), we shift the Fermi surfaces in the opposite direction (electrons have a negative charge). Charge current along the x-axis is launched due to the application of the electric field. We can observe in the illustration that the reason for the current flow would be that a bigger part of the Fermi surface lies in the right half-plane (from the y-axis); hence most conduction electrons have k_x positive. This is the situation in the right column of this figure. Because the Fermi surfaces differ for spin-up (red curves) and spin-down (blue curves) electrons, the respective currents for electrons with corresponding spin orientations $\boldsymbol{j}_\uparrow$, $\boldsymbol{j}_\downarrow$ are different and thus $\boldsymbol{j}_s = \boldsymbol{j}_\uparrow - \boldsymbol{j}_\downarrow \neq 0$. The orientation of the Fermi surfaces taken relative to our chosen coordinate system represents the different crystallographic orientations of RuO_2 lattice to the current. a) Charge current flows along the $[1\bar{1}0]$ direction. The Fermi surfaces for different spin orientations have different dimensions in the x-direction, so there is a spin current along the same axis as the charge current—the current is spin polarised. (In the illustration, we assume the momenta of spin-up electrons are mostly higher.) b) Charge current flows along the $[0\bar{1}0]$ direction. The Fermi surfaces for different spin orientations differ in the y-direction so a spin current, perpendicular to the charge current, is present.

2.3 Terahertz spectroscopy

When we speak of the terahertz spectral region, we mean electromagnetic radiation with frequencies approximately from 0.1 to 30 THz (which corresponds to wavelengths from about 3 mm to 10 μm)[3]. From an experimental perspective, one of the specifics of the THz spectral region is that, unlike in optical, infrared or ultraviolet regions, electric field E is often measured rather than intensity I. This means that measurements of THz pulses contain complete phase information. The direct measurement of the electric field is possible because the changes of the electric field in time are much slower when compared to the fields of optical electromagnetic waves [21].

THz radiation is emitted via processes described in sections above and by measuring the THz emission, we can study the THz spin currents in materials. We detect emitted THz waves by a method called *electro-optical sampling* (EOS). This method is based on the Pockels effect [21]. It is a linear electro-optical effect that occurs in certain crystals without a centre of symmetry [22]. When light passes through the crystal in an external electric field $\boldsymbol{E}$, the phase between two perpendicular components of the electric field of light changes. This change is linearly dependent on the amplitude of the external electric field E. In the electro-optical sampling method, the polarisation of optical laser pulse with a much higher frequency gets modified in electro-optic crystal by the Pockels effect where the external electric field is the electric field $\boldsymbol{E}_{\mathrm{THz}}$ of THz wave incident on the crystal. Thus, the change of phase is proportional to E_{THz} and by measuring this phase difference and time-delaying the laser pulse (*probe*) relative to THz pulse, we are able to reconstruct the whole THz pulse electric field $E_{\mathrm{THz}}(t)$. The EOS method is illustrated in Fig. 2.6. Let us note that in our laboratory setup, the electro-optic crystal is oriented in such a way that only the horizontal part of the electric field induces the phase difference of polarisations (illustrated in Fig. 2.5).

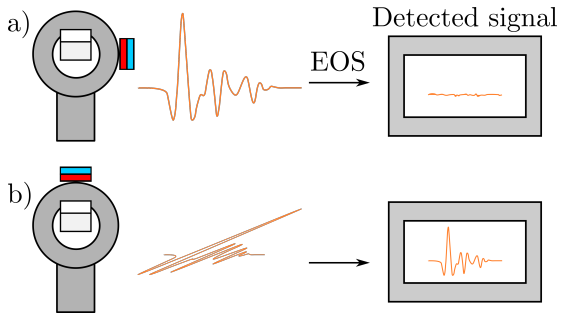

Figure 2.5: Illustration of the EOS detection dependence on THz wave polarity. The THz wave is emitted from an STE with its FM layer magnetisation controlled by a permanent magnet. a) A linearly polarised wave in the vertical direction is emitted from the STE; thus, no THz waveform is detected by EOS in our experimental setup. b) A horizontally polarised wave is emitted from the STE and is detected by the EOS detection.

[3]Sometimes term *terahertz window* is used. There is no exact and universal definition of THz spectral region. This interval is taken from [21], whereas in the article [4], the frequency interval mentioned is 0.3-30 THz.

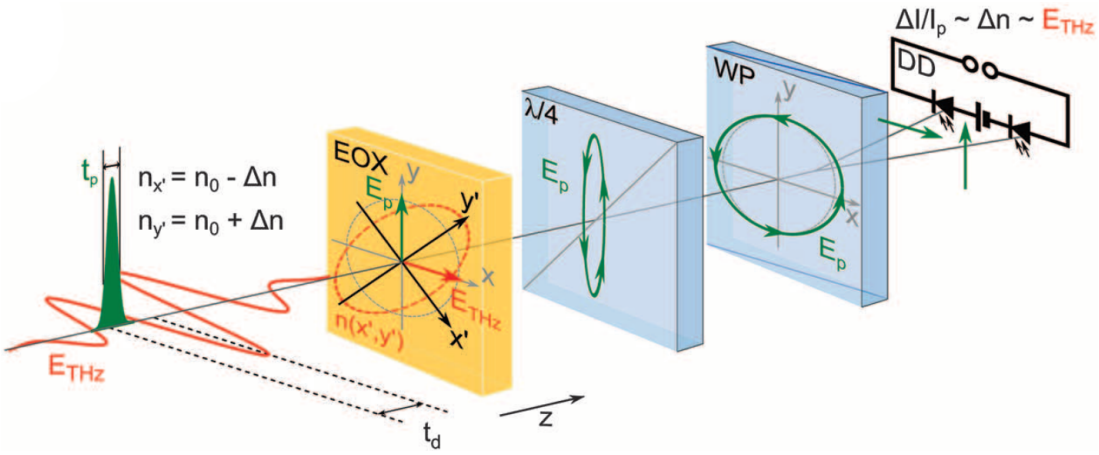

Figure 2.6: Schematic illustration of detection of THz radiation using EOS. The linearly polarised probe laser pulse (green) is incident on the electro-optic crystal (EOX) simultaneously as a THz pulse. In the electro-optic crystal, the polarisation of probe light changes from linear to elliptical polarisation with large eccentricity. Then it passes through a quarter-wave plate ($\lambda/4$) where polarisation changes to almost circular and then two perpendicular polarisation components are separated in a Wollaston prism (WP). These are detected by a pair of photodiodes and the difference between the measured currents is proportional to E_{THz}. We reconstruct the whole THz pulse $E_{\mathrm{THz}}(t)$ by delaying the probe laser pulse from the THz pulse. Taken from [23].

2.4 Laboratory setup for THz wave generation and detection

For measurements, we used the laboratory setup at the Laboratory of THz spintronics at the Faculty of Mathematics and Physics which is schematically shown in 2.7. For THz wave generation, we excite the samples by an optical laser (*pump*) pulse, causing them to emit THz radiation due the effects described in previous sections. Detection is accomplished by electro-optic sampling, as discussed in previous section.

We utilise an optical *chopper* with a frequency of 1468 Hz to reduce the 1/f noise. 1/f noise, also called *flicker* noise, is a commonly used term for random fluctuations with amplitude dependence on frequency (of observed signal) close to 1/f [24]. This type of noise is notably present in electronics, therefore, in our detectors as well. To reduce its impact on our measurements, the laser beam passes through a chopper, a device akin to a fan—its wings stop and permit the propagation of the beam at a constant frequency. This makes the signal we are interested in observable at the frequency of the chopper while the 1/f noise remains large at lower frequencies so its effect on the acquired data is less significant.

For laser beam generation, we use the PHAROS-10W-SP-1mJ femtosecond laser system which can generate femtosecond laser pulses with a central wavelength of 1030 nm, tunable pulse energy (up to 1 mJ), tunable pulse repetition rate (10 kHz – 1 MHz) and tunable pulse duration (190 fs – 20 ps). To delay the probe pulse and the THz wave, we use an optical *delay line* by

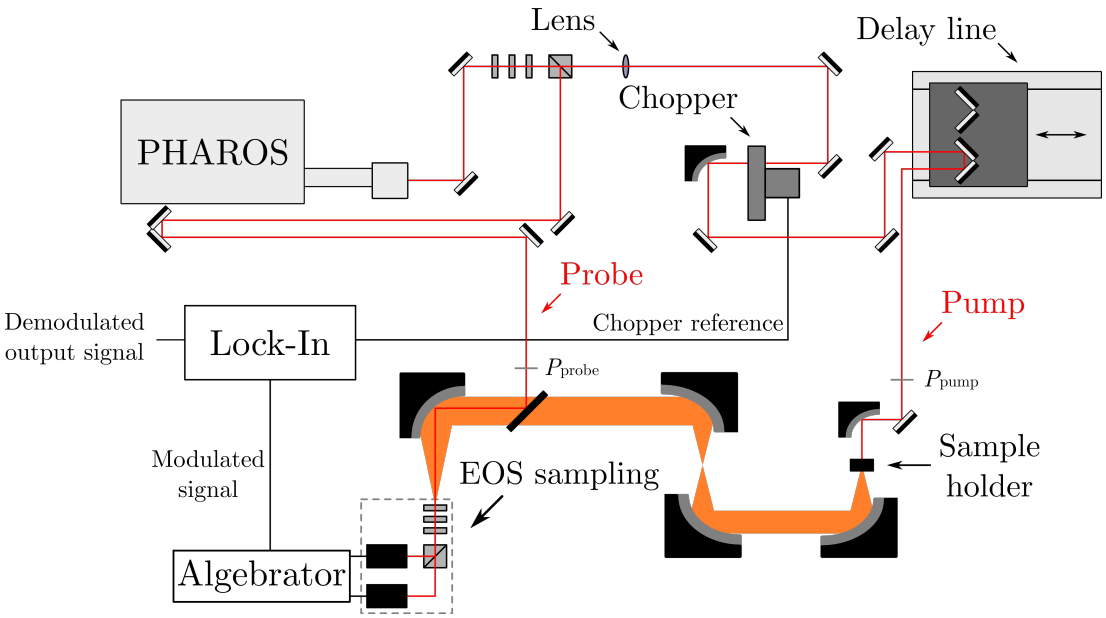

Figure 2.7: Schematic illustration of the laboratory optical setup. The laser pulse (red) is split in the setup into two beams: pump and probe. Then, the pump pulse passes through a lens with a focal length of 2 m. To reduce noise, the pump pulse is modulated by an optical chopper. After passing through the chopper, the pump beam is reflected off several mirrors, including a pair of mirrors on an optical delay line which can move the pair, shortening or prolonging the pump pulse optical path. The pump pulse is ultimately reflected off a parabolic mirror at the sample/THz emitter. The emitted THz wave is guided by a set of parabolic mirrors to an electro-optic GaP crystal. There it propagates along the probe beam, which gets elliptically polarised in the GaP crystal by the Pockels effect and then split into two linear polarisations by a quarter-wave plate and a Wollaston prism. The electric signals from the two polarisations detected are subtracted in the algebrator. Lastly, the electric signal from the algebrator, modulated by the chopper frequency, is demodulated in a Lock-In system. Points where the powers of pump and probe beams have been measured are annotated by P_{pump} and P_{probe}.

which we vary the optical path of the pump pulse. By moving a pair of mirrors on the delay line, we can measure the electric field of the THz wave emitted at a chosen point in time[4]. The laser is focused on the sample by a 0.5 D lens onto a spot with FWHM 280 μm. For electro-optical sampling, we use a 2 mm GaP crystal. To demodulate the chopper-modulated signal, we use the SR830 Lock-In amplifier.

In our experiments, we used the laser with the frequency of pulses 10 kHz, laser attenuated to 30% of maximum laser power (2 W) and the beam power was additionally lowered by optical components (half-wave plate and polarisator) in the optical path. The powers of pump P_{pump} and probe beam P_{probe} have been measured before the sample holder and the detection in GaP crystal,

[4]We implicitly assume that THz waves emitted during the experiment are almost equal and that from measurements of many emitted THz waves at distinct phases we can reconstruct the THz wave.

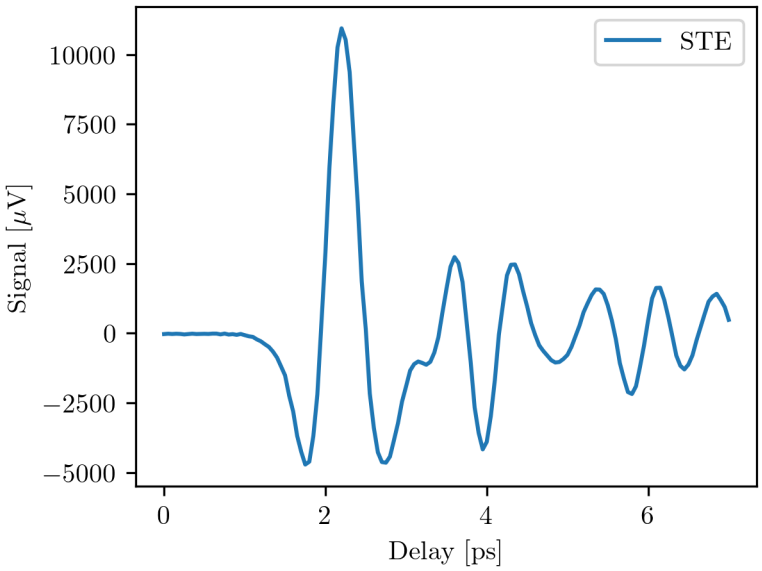

Figure 2.8: The THz wave emitted by an optimised STE (CoFeB/Pt). The measured voltage from Lock-In is plotted against the controlled delay of the pump beam. In the graph, we can observe multiple oscillations. The STE emits only a pulse with one oscillation of the electric field and the other waves measured are the results of reflection at water vapours in the laboratory. (The original THz wave ends at about 3 ps.)

see Fig. 2.7. For detection, we used pulses with $P_{\text{probe}} = 700$ μW and for sample excitation, we first used $P_{\text{pump}} = 1.5$ mW but slowly increased the power of the pump beam to acquire greater signals (exact values are given in the section with measurement results). The measurements were done under room temperature, atmospheric pressure and humidity. We used $P_{\text{pump}} = 18$ mW for measurements with optimised STE – a CoFeB(2 nm)/Pt (2 nm) heterostructure (the lengths in parentheses indicate the thickness of the layers) which was previously manufactured for general-purpose THz generation in the laboratory.

In measurements, we changed the delay of the pump pulse on the delay line and measured the voltage given by the Lock-In amplifier ("Signal" in graphs), which corresponds to the differential signal from detecting photodiodes. For each point in a graph, we read out the averaged voltage, usually over a 210 ms time period. Measurements typically consist of 140 evenly spaced points corresponding to steps taken by the delay line. We changed the number of points in a graph in cases when the measurement would be too time-demanding. As the delay is relative, we set the delay of the first point measured as zero in graphs. For an example of measured THz waveform, see Fig. 2.8. In graphs, we also offset the signal voltages so the mean of the measured voltages is precisely zero.

2.5 Sample growth

For our work, nine different multi-layered samples were grown. As a substrate material, we chose TiO_2 on which RuO_2 layers were deposited by pulsed laser deposition. On the RuO_2 layer, Pt or CoFeB were deposited by sputtering (CoFeB—a ferromagnetic material, Pt—a nonmagnetic material with large

reported spin Hall angles [12]). Before moving on to describe the manufactured samples in more detail, we will briefly explain the growth methods.

Pulsed laser deposition (PLD) [25] is a thin film growth method belonging to a family of physical vapour deposition methods where atoms, molecules and other particles (collectively called *species*) from source material in solid phase are ejected and travel to the substrate. This process takes place in low-pressure environments (usually an inert gas) for the mean free paths of ejected atoms to have macroscopic orders of magnitude and to avoid deposited film contamination. In PLD, the source material is *ablated* (i.e. removed) from the *target* by intense laser pulses. The ejected species form a cloud of plasma (*plasma plume*) which travels to the heated substrate where the source material is deposited, slowly forming a thin film. This method enables high control over deposition parameters and allows for deposition at a wide range of pressures ($10^{-6} - 10^{-9}$ mbar) [25].

Sputtering is another physical vapour deposition method where a different approach to extracting atoms from a source material (target) is utilised. As in PLD, two materials (the source material which we want to deposit and the substrate on which we grow the thin film) are put into a low-pressure chamber which is filled with rare gas (usually Ar is chosen for its chemical inertness, low cost and other favourable attributes). A constant or alternating voltage at radio frequencies is applied between the target and the substrate. Ionised atoms of the gas are then accelerated towards the target which causes the target atoms to be expelled (*sputtered*) from the material. The sputtered atoms condense at the substrate and form layers of the thin film [26].

The RuO_2 layers have been grown *epitaxially* on TiO_2, meaning that, as a result of similar lattice parameters and structure, the orientation of crystallographic axes relative to the surface of RuO_2 is determined by and equal to the TiO_2 crystal orientation (relatively to the surface). This principally allows us to study the THz emission from RuO_2 by virtue of the different described processes of the THz radiation generation.

2.6 Sample multilayers

The samples were in the form of 5 mm $\times$ 5 mm thin squares, most of the material being the $\sim$ 0.5 mm thick TiO_2 substrate on which thin films were deposited (although only on a segment of the square, see Fig. 2.9). RuO_2 layers of approximately 18 nm thickness were deposited by PLD on the TiO_2 substrate by Gabriele de Luca from The Catalan Institute of Nanoscience and Nanotechnology and The Institute of Material Research of Autonomous University of Barcelona. The epitaxial growth of RuO_2 layers has been confirmed by x-ray diffraction performed by Gabriele de Luca. Afterwards, 3 nm layers of Pt or/and CoFeb have been grown by sputtering by Daniel Scheffler from Technical University Dresden. In table 2.1, the manufactured samples are listed. Samples were grown in three orientations of RuO_2 crystal relative to the surface. We indicate the orientation by writing the orientation of the interface (relative to RuO_2 crystal axes) in parentheses[5]. The orientations are:

[5]Our notation and chosen labelling of RuO_2 layer orientation coincide with labelling used in [5] from which we have used illustrations 2.2 and 2.3. However, our choice of crystallographic

- (100) → where we expect the appearance of spin current perpendicular to charge current flowing along [100] and thus THz radiation from the sample capped with CoFeB
- (110) → where we expect spin polarisation of charge current flowing along [110] and thus THz radiation from the sample capped with Pt
- (001) → where symmetries in RuO_2 forbid spin currents originating from charge current in direction [001], and in exchange interaction, thus we expect no THz radiation associated with effects connected to the exchange interaction in altermagnets

Table 2.1: Prepared samples. The first column gives the sample name under which the samples will be referenced. In the "Substrate" column, the orientation of the lattice to the surface is given in parentheses, which denotes the direction perpendicular to the surface (and layer interface). The "First layer" column lists the layer grown by Gabriele de Luca, "-" denotes that no RuO_2 layer was grown on the samples. The last column gives the second layer grown by Daniel Scheffler. The lengths in parentheses indicate the layer thickness.

Sample name	Substrate	First layer	Second layer
ln10a	TiO_2 (100)	RuO_2 (18 nm)	Pt (3 nm)
ln10b	TiO_2 (100)	RuO_2 (18 nm)	CoFeB (3 nm)
ln10c	TiO_2 (100)	-	CoFeB (3 nm) / Pt (3 nm)
ln10d	TiO_2 (110)	RuO_2 (18 nm)	Pt (3 nm)
ln10e	TiO_2 (110)	RuO_2 (18 nm)	CoFeB (3 nm)
ln10f	TiO_2 (110)	-	CoFeB (3 nm) / Pt (3 nm)
ln10g	TiO_2 (001)	RuO_2 (18 nm)	Pt (3 nm)
ln10h	TiO_2 (001)	RuO_2 (18 nm)	CoFeB (3 nm)
ln10i	TiO_2 (001)	-	CoFeB (3 nm) / Pt (3 nm)

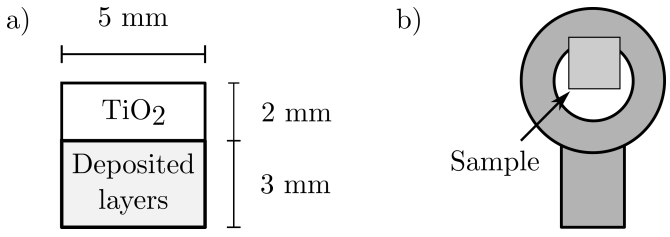

Figure 2.9: a) Illustration of manufactured samples from the front side. Part of the substrate has been left uncovered by deposited layers for reference and for easier manipulation with the samples—the samples were glued by double-sided tape to the holder with the tape glued solely to the TiO_2 substrate part of the sample. b) Illustration of sample attached to the sample holder. The sample is shown as much larger relative to the sample holder than in reality for clarity.

directions in RuO_2 is different. It is effectively equivalent to the choice of directions in [5] due to rotation symmetries present in RuO_2.

2.7 Superconducting quantum interference device (SQUID)

For the measurement of magnetic moments of the multilayers, we used superconducting quantum interference devices, shortly called SQUIDs [27]. These devices are based on the properties of superconducting materials and Josephson junctions. The SQUID device consists of two superconducting electrodes in the shape of an annulus. The superconducting electrodes are separated but weakly linked (layer of insulator thin enough to permit tunnelling across, point contact, etc.); the points of separation are called Josephson junctions.

Let us briefly explain the working principle of dc SQUIDs. When a superconducting material is enclosed in a loop (SQUID without Josephson junctions), any magnetic flux through the enclosed area causes the material to react in such a manner that a current is generated in the material, which reduces the magnetic flux to zero or to an integral multiple of magnetic flux quantum[6] $\Phi_0 = \frac{h}{2e}$. The same effect occurs in SQUIDs where the superconducting current creating opposing magnetic flux flows through the Josephson junctions. If we make current flow through a SQUID then at a certain critical current I_C, we measure a voltage across the SQUID. For magnetic field measurement, we maintain a *bias current* higher than I_C flowing through the SQUID and measure the voltage across. This voltage periodically increases and decreases if there is magnetic flux inside the annulus because an additional *screening current* flows through the annulus to oppose the change of magnetic flux so that flux enclosed by the annulus is an integer multiple of Φ_0. The screening current increases at first but when the magnetic flux is exactly between two adjacent multiples of Φ_0, the current changes sign and its amplitude decreases until the flux is precisely a multiple of Φ_0. This results in measured voltage showing minima when the external magnetic field creates flux which is an integer multiple of Φ_0 and maxima exactly in the middle between the minima.

[6]This can be understood as the effect on electron pairs in the superconducting material whose wavefunctions differ only in phase which is dependent on position in the material $\psi = \psi_0 e^{i\phi(\boldsymbol{r})}$. (That this wavefunction describes all superconducting electrons in the material stems from the description of superconductivity.) The magnetic field inside an annulus from superconducting material must change the wavefunction (if superconductivity is to be preserved) in such a way that the change of phase around the annulus is an integer multiple of 2π. If this were not the case, the wavefunction describing electrons in the superconductor would be discontinuous at some point.

3. Measurement results

Most of the laboratory work regarding THz spectroscopy has been carried out with the assistance of my colleague Jiří Jechumtál at the Laboratory of Opto-Spintronics at the Faculty of Mathematics and Physics of Charles University at Karlov. We also cooperated with dr. Kamil Olejník, who field cooled some of the samples and ran SQUID measurements at the Institute of Physics of the Czech Academy of Sciences at Cukrovarnická.

3.1 SQUID measurements

Along with spectroscopic measurements at the THz laboratory at Karlov, the dependence of magnetic moments of samples containing CoFeB on the applied magnetic field has been measured. For these measurements, SQUID magnetometer MPMS XL at Cukrovarnická has been used. The measurements were made at room temperature, the magnetic field was applied in the plane of sample layers, and the magnetic moment was measured in the same direction.

The magnetic moment of sample ln10f [CoFeB/Pt on TiO_2 (110)] has the characteristic hysteresis loop of a ferromagnetic material (see Fig. 3.1). The magnetic moment is of the order of tens of $nA{\cdot}m^2$. The magnetic moment of ln10f has been measured in two different orientations of the sample layers relative to the field applied.

The magnetic moments of samples ln10b, ln10e, ln10h, i.e. RuO_2/CoFeB in different crystallographic orientations have also been measured (see Fig. 3.2). We can observe that the substrate orientation has an impact on the shape of the hysteresis curve for the sample. What has been a surprise for us is the magnitude of the magnetic moment, which is about ten times lower than in the case of the reference CoFeB/Pt sample (ln10f).

For the sample ln10e, multiple measurements were made where the sample had been first put into a magnetic field of 5 T and then into lower fields with an opposite polarity. After, we measured the magnetic moment of the sample for a low interval of the magnetic field applied. The results of these measurements are shown in Fig. 3.3 and confirm the exchange interaction between RuO_2 and CoFeB layer resulting in exchange bias (the characteristic horizontal shift of the hysteresis loop is visible) and its amplitude is roughly 3 mT.

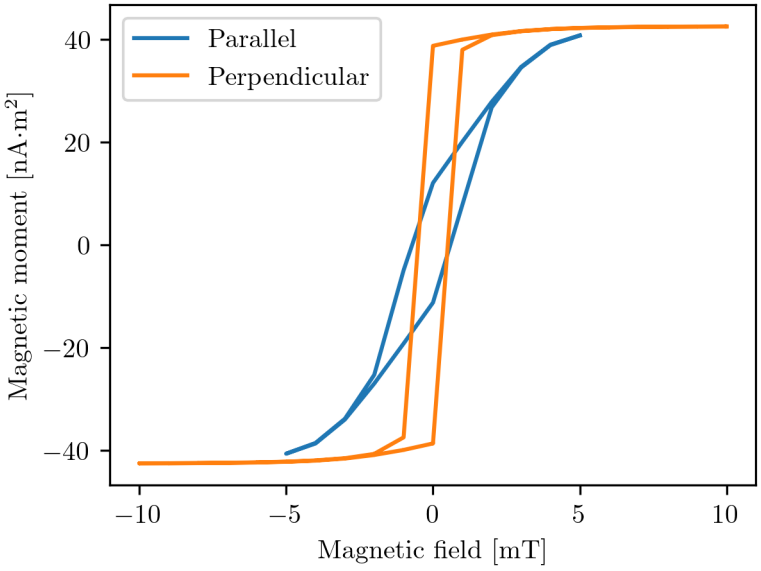

Figure 3.1: SQUID measurement of dependence of magnetic moment on applied magnetic field for sample ln10f [CoFeB/Pt on TiO_2 (110)]. The sample has been put into the SQUID in two orientations—in an orientation where the field applied is parallel to the plane of layer interface and in an orientation where the field is perpendicular to the field. The linear paramagnetic contribution of the substrate has been fitted and subtracted from the measured magnetic moment.

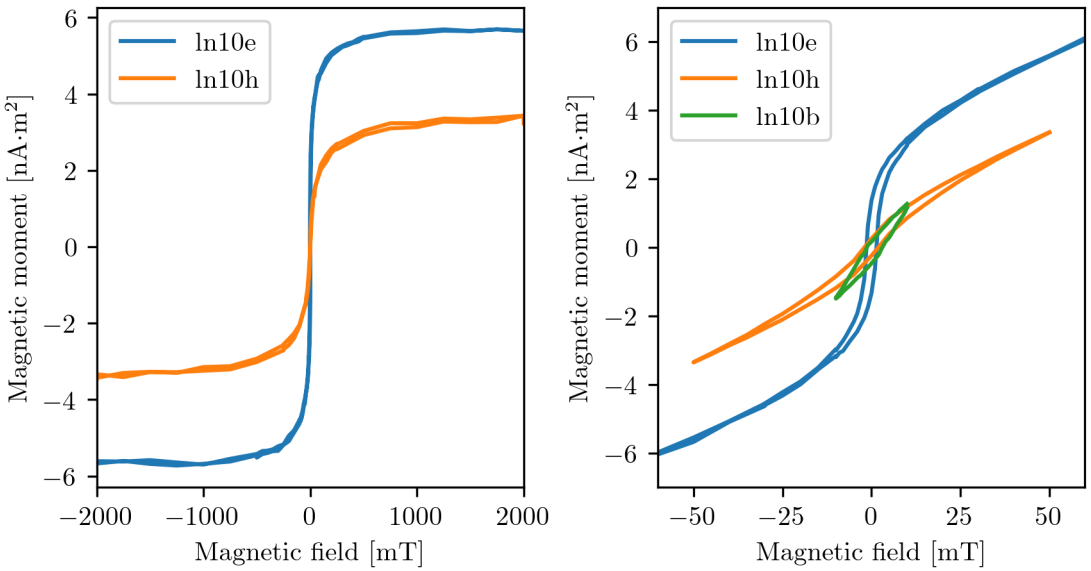

Figure 3.2: SQUID measurement of dependence of magnetic moment on applied magnetic field for sample ln10e, ln10h and ln10b [RuO_2/CoFeB on TiO_2 (110), (001) and (100)]. In the graph on the left, the linear contribution of the substrate to the magnetic moment has been fitted and subtracted. On the right, we show the magnetic moment measured by the SQUID. In this case, we do not subtract the linear relationship because the measurement made for the sample ln10b was not measured in sufficiently high fields for the linear contribution to be dominant.

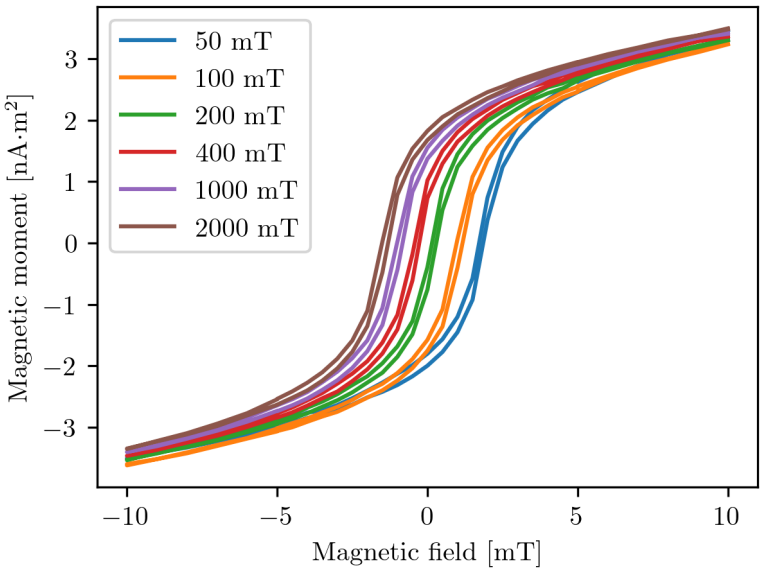

Figure 3.3: SQUID measurements of the magnetic moment of the sample ln10e and its dependence on magnetic field applied. The measurements shown are made after putting the sample in a magnetic field of -5 T (the minus sign here denotes that this field had opposite polarity from the fields given in the graph legend) then in fields of various strengths, turning off the field and then measuring the response of the sample to applied fields lower than 10 mT. The curves measured are labelled by the field applied to the sample before measuring the curve.

The main and most interesting result from the SQUID measurements is the ten times lower magnetic moment of RuO_2/CoFeB samples. The hysteretic loops are shifted by exchange bias on the order of mT and the magnetic coercive field[1] is of similar magnitude. The lesser magnetic moment, we might interpret as the CoFeB layer being damaged or the growth of this layer not coming out properly. It can be an effect related to the interface of RuO_2 and CoFeB being more rough, inhomogeneous or structurally damaged than we imagine. However, we observe a non-zero exchange bias that hints at the interface being, at least in some regions, sufficiently smooth and epitaxially grown for observable exchange bias to occur. Perhaps the CoFeB layer is much thinner than we predict. Then, some thinner parts of the CoFeB might be exchange-coupled to the RuO_2 with such strength that the magnetic fields of the SQUID do not change their magnetic moments. Other thicker parts might not be coupled so strongly and align their magnetic moments with the applied field.

To summarise, samples with RuO_2/CoFeB layers do not have the expected properties. This might explain the results of spectroscopic measurements which will be presented in the following sections.

[1]Magnetic field at which the magnetic moment switches its direction.

3.2 CoFeB/Pt reference sample

The sample ln10c (CoFeB/Pt), which we will hereafter refer to as the reference sample, has been used for THz generation first to confirm that the experimental setup works using the conventional STE device materials (CoFeB/Pt in this case). We put the reference sample into the focus of the pump laser pulse and put a permanent magnet on top of the sample holder to control the magnetisation of the ferromagnetic CoFeB layer. We put the sample in the sample holder so the laser first propagates through the optically transparent substrate and then the THz wave from the metallic layer is emitted to the free space. In measurements of THz pulses (Fig. 3.4), we have confirmed that a THz pulse is emitted from the reference sample and that the THz electric field changes sign when the magnetisation of the sample is inverted. In the graph below, we denote amplitudes of measured signals for comparison. The amplitude is calculated as the difference between the maximum and minimum signal values of the measured THz waveform.

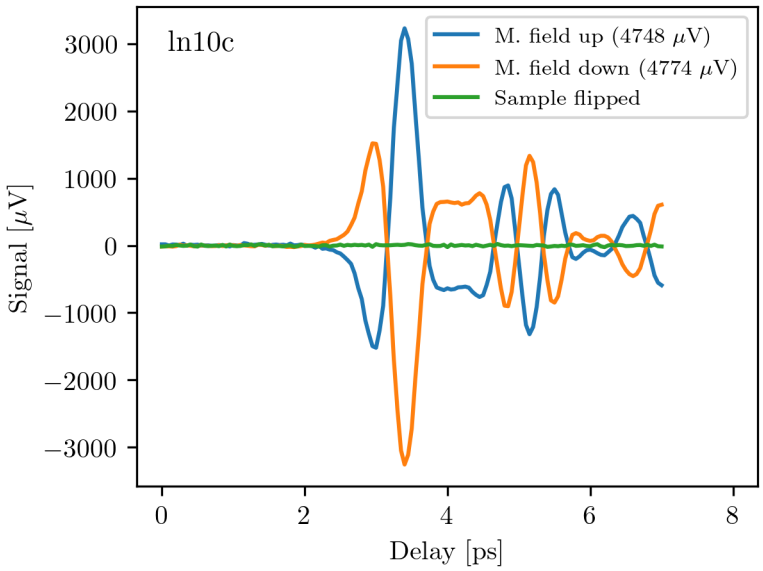

Figure 3.4: THz signals from the reference sample (ln10c). We measured the signal from the reference sample with CoFeB layer magnetisation controlled by a magnet put on the sample holder. The signals shown are from measurements where the magnet was put on the top of the sample holder (magnetic field pointing "up") and then the magnet was rotated so the magnetic field would point in the "down" direction. The third measurement was taken after flipping the sample. We denote amplitudes of measured signals in parentheses.

Furthermore, we observed that we detect no signal when we rotate the sample around an inplane[2] axis (flip the sample) so the THz wave travels through the TiO_2 substrate and the laser pulse is first incident on the CoFeB/Pt bilayer. (The THz wave generated propagates in both directions when the substrate used in STE is transparent for THz radiation.) This led us to the suspicion that the substrate is not transparent for THz radiation and we have confirmed so by using the optimised STE (CoFeB(2 nm)/Pt(2 nm)) and putting the reference sample

[2]Inplane meaning in a plane of the interface.

in the path of the emitted THz pulse because no signal above noise from the STE has been detected. For this reason, all of the following measurements are made so the detected THz wave propagates only through the metallic layers and not through the substrate.

3.3 RuO_2 samples with CoFeB layer

After the initial measurements of THz radiation from the ln10b sample [RuO_2 (100)/CoFeB] sample, we have increased the pump laser beam power P_{pump} gradually from 1.5 mW up 30 mW since only noise has been detected after one loop[3]. No apparent damage was visible on the sample and thus we used $P_{\text{pump}} \approx 20$ mW for further experiments with other samples containing RuO_2. With experiments on the RuO_2 samples containing the CoFeB layer, we wanted to distinguish the component of the potential THz emission related to the altermagnetic processes. Therefore, we measured emission with various orientations of the sample in the holder and different magnetisation of the ferromagnetic layer. (For the orientation of the sample in the holder, see Fig. 3.5; the exact measurements will be described later in the text.) We expected the magnetism-related signal to change sign with the inversion of the magnetic field, same as for the reference sample (Fig. 3.4), and when the magnetisation is horizontal or the sample is rotated horizontally, we expected no signal because the EOS detection measures fields only in the horizontal direction. (The emitted THz wave is linearly polarised so if rotating the sample or the magnetisation rotates the polarisation, no signal is detected.)

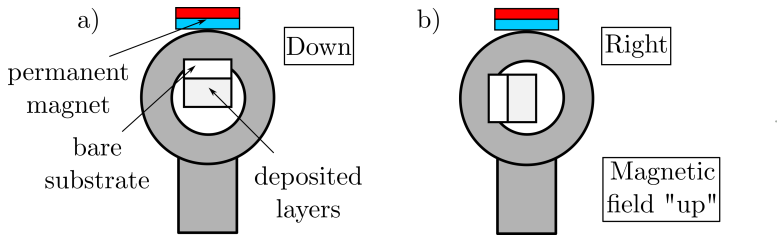

Figure 3.5: Schematic illustration of the positioning of sample bilayer in the sample holder and of the permanent magnet. The sample and the magnet are shown as much larger relative to the sample holder than in reality for illustrative purposes. The samples are pictured from the direction of emitted THz radiation, meaning that the generation beam hits the sample from behind in this illustration. In the thesis, we denote the orientation of the samples by the direction of the part of samples where layers of RuO_2, CoFeB and Pt are deposited relative to the part with bare TiO_2. Two orientations are shown, the orientation of the magnetic field generated by the permanent magnet is "up" (corresponding to the notation "+" used for later graphs in the text). a) "Down" orientation of the sample. b) "Right" orientation of the sample.

In the following subsections, we will describe the THz emission from all the samples, although we mainly focused on the ln10b sample since the theory

[3]One loop meaning one measured waveform from delaying the probe and the generating pulse.

predicted the spin-splitting effect to be the most efficient (relatively) for generating THz radiation. Before conducting the actual measurements, all samples were put in a strong magnetic field of 12 T at Cukrovarnická in an effort to homogenise the magnetic structure of RuO_2[4].

To affect the magnetisation of the CoFeB layer, we used mainly two sources of magnetic fields. Initially, we used a permanent magnet which we put on the metallic sample holder; the magnetic induction near the sample was measured by a gaussmeter to be approximately 10 mT. Later, we measured the emission from the samples put in a Halbach cylinder[5] where we measured induction 200 mT in the centre.

3.3.1 Samples ln10e and ln10h

At first, we measured the THz emission from the samples in the 10 mT field generated by the permanent magnet on the sample holder. According to the SQUID measurements, this magnetic field was expected to be strong enough to manipulate the FM magnetisation freely. In a single measurement of a THz waveform, there was only noise observed, therefore, we repeated the measurements of a waveform for several loops[6] for subsequent measurements of THz radiation from samples with RuO_2.

From samples ln10e [RuO_2 (110)/CoFeB] and ln10h [RuO_2 (001)/CoFeB], we expected no THz emission and, indeed, we measured seemingly no signal from them in the field of 10 mT, see left panels (a) in Figures 3.6 and 3.7. For these measurements, we put the permanent magnet on top and measured the emission from two sample orientations. For sample ln10h, we also tried flipping the permanent magnet so the magnetic field is inverted. After putting the samples in the Halbach cylinder, we measured the emission in the same orientations (panels (b)). Since we observed non-zero signals in stronger magnetic fields, we also measured signals from the samples after inverting the polarity of the applied magnetic field. For both samples, we can observe that the measured curves show a small but clear THz emission (of amplitudes 4.6 μV - 5.7 μV) which is slightly higher than the noise. This is visible for both orientations of ln10e in the cylinder and for the upward orientation of ln10h and field pointing down in the cylinder. Another interesting finding from the measurements is that the THz emission from horizontally (right or left) oriented ln10e increased substantially in the higher magnetic field and the peak is at a different delay (about 1.8 ps) than for every other THz wave measured (they are at about 1.5 ps delay).

[4]According to ref. [20], a magnetic field of the magnitude of 12 T is not strong enough to reorder the magnetic structure of RuO_2. This fact was unknown to us at the time when the experiments were carried out.

[5]A ferromagnetic cylinder or an array of permanent magnets with the magnetisation of the magnetic component(s) oriented in such a way that a strong magnetic field is in the centre of the cylinder and zero field is outside of it [28].

[6]The number of loops was mostly limited by the time that a given measurement lasted. We always tried to measure long enough for the signal to be visible above the noise.

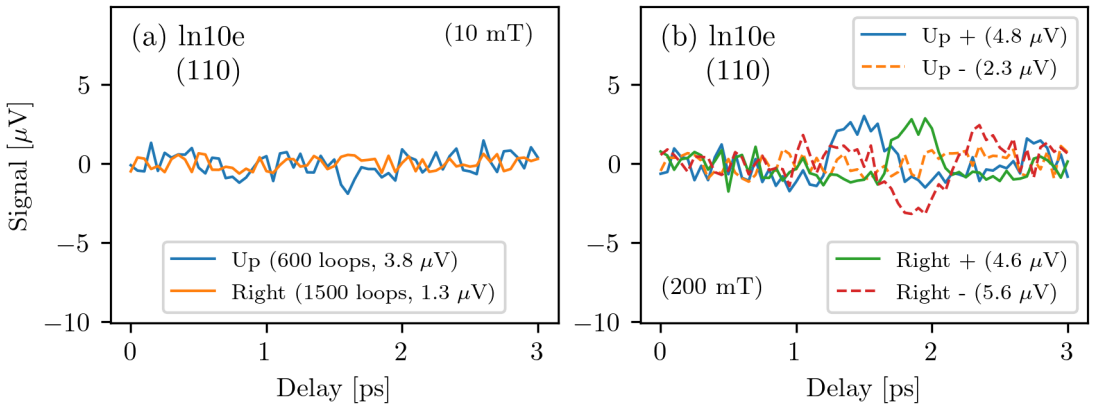

Figure 3.6: Graphs of measured signals from sample ln10e [RuO_2 (110)/CoFeB]. In the graph legend, numbers in parentheses indicate the amplitude of the signal and in (a) the number of loops averaged for the shown curve. We measured the emission for the two orientations of the sample using the notation as described in Fig. 3.5. The relative crystallographic orientation of TiO_2 is written under the sample name. (a) Measurements of emission where the permanent magnet (10 mT) was on top of the sample holder. (b) Measurements of emission where the sample was put in the Halbach cylinder (200 mT). The curves are averaged over 450 loops. For each orientation of the ln10e sample, we measured emission for two opposite directions of the magnetic field. The field was always applied to the sample vertically, "+" denotes the field in the cylinder directed upwards and "-" denotes the field in the opposite direction.

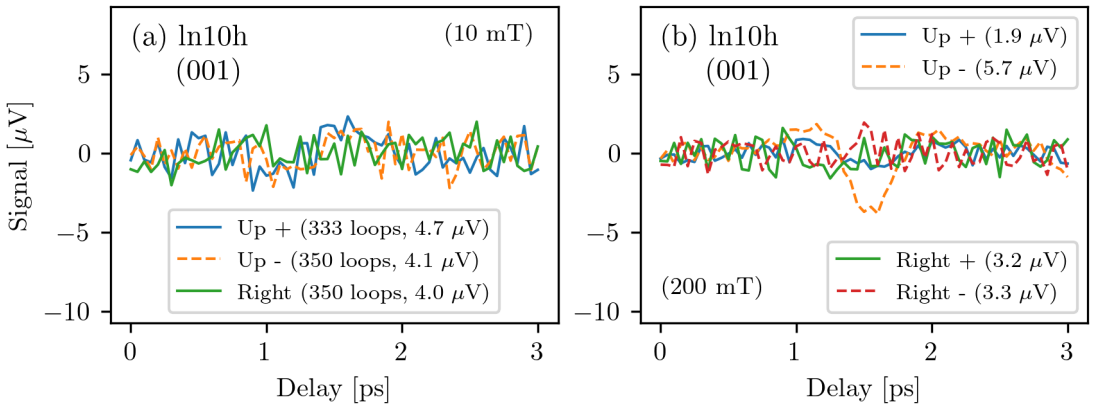

Figure 3.7: Graphs of measured signals from sample ln10h [RuO_2 (001)/CoFeB]. Labelling of the curves in the graph is the same as for 3.6. (a) Measurements of emission where the permanent magnet (10 mT) was on top of the sample holder. We measured the emission twice for the sample in the "up" orientation, with the magnetic field pointing up and down. (b) Measurements of emission where the sample was put in the Halbach cylinder (200 mT). The curves are averaged over 450 loops.

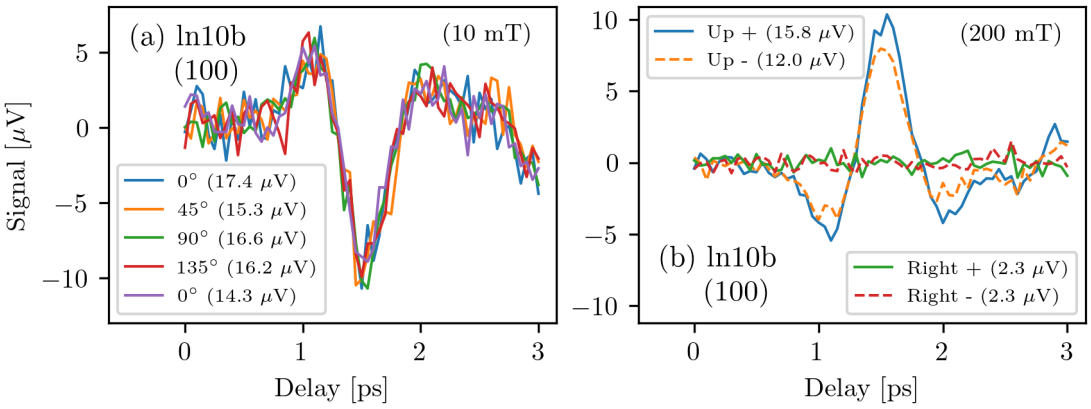

Figure 3.8: Graphs of measured signals from sample ln10b [RuO_2 (100)/CoFeB]. Numbers in parentheses indicate the amplitude of the measured signal. (a) Measurements of emission where the sample has been oriented downwards and the permanent magnet was put around the sample holder at different angles. We label the shown curves by the angle between the on-top position of the magnet and the position of the magnet for the given measurement. We measured emission from the sample with the magnet on top twice, as the first and last measurements. The curves are averaged over 100 loops. (b) Measurements of emission where the sample was put in the Halbach cylinder (200 mT). Plus or minus signs indicate the polarity of the vertically applied magnetic field. The curves are averaged over 450 loops.

3.3.2 Sample ln10b

We measured THz radiation from the sample ln10b [(]RuO_2 (100)/CoFeB] put in the 10 mT magnetic field of the permanent magnet and in the 200 mT magnetic field of the Halbach cylinder. We measured the emission of the sample in different positions of the magnet on the sample holder (Fig. 3.8, panel (a)) and with the Halbach cylinder, we measured the emission for different orientations of the sample and opposite magnetic fields in the vertical direction (Fig. 3.8, panel (b)).

In low magnetic fields (panel (a)), we observe signals with amplitudes higher than 14 μV for the vertical (up or down) orientation of the sample. When we gradually rotated the 10 mT magnetic field by putting the magnet on different spots on the sample holder, we found that the orientation had possibly only a negligible effect on THz emission. However, these measurements were short (only 100 loops have been averaged) so the differences could be mostly obscured by noise. From the measurements in the Halbach cylinder (panel (b)), we note that there is an observable difference in the signal for the opposite directions of the magnetic field for the vertical orientation of the sample while we do not observe any discernible signal for the horizontal orientation.

3.3.3 Magnetic and nonmagnetic signals

To quantify how much of the signal is of magnetic origin[7], we take a difference of signals measured for two opposite directions of applied magnetic field S_+, S_- and divide it by two:

$$S_{\text{mag}} = \frac{S_+ - S_-}{2}, \tag{3.1}$$

where S_{mag} denotes the magnetic signal. We get signals of nonmagnetic origin S_{non} by taking the sum of S_+, S_- and dividing by two:

$$S_{\text{non}} = \frac{S_+ + S_-}{2} \tag{3.2}$$

We consider the signal of magnetic origin important because, for the sample ln10b, the emission mechanism should be dependent on the magnetisation of the ferromagnetic layer (specifically the spin polarisation of current from the ferromagnetic layer). We show the magnetic signals and nonmagnetic signals in Fig. 3.9 for samples in the Halbach cylinder (same measurements as shown and discussed above).

In the graphs for magnetic signals, we can see a magnetic signal with a peak located at a delay of approximately 1.5 ps for all samples. This magnetic signal even has a similar amplitude for every sample, therefore we might associate this signal with the same process for every crystal growth orientation. No magnetic signal seems to be present for the horizontal orientation of the samples ln10b and ln10h. Therefore, we can conclude that the magnetic signal does depend on the crystal rotation but not on the growth direction. Also, we can see that for ln10e, a magnetic signal (greatest magnetic signal measured) is present and has a peak around delay 2 ps.

For nonmagnetic signals, we observe a signal of substantial amplitude for sample ln10b in the vertical orientation. For the other two samples, a much lower signal is present for the vertical orientation. In the horizontal orientation, none of the samples shows recognisable THz signals.

[7]Or, specifically, how much of the signal is dependent on the magnetisation of the ferromagnetic layer which we affect by the applied magnetic field.

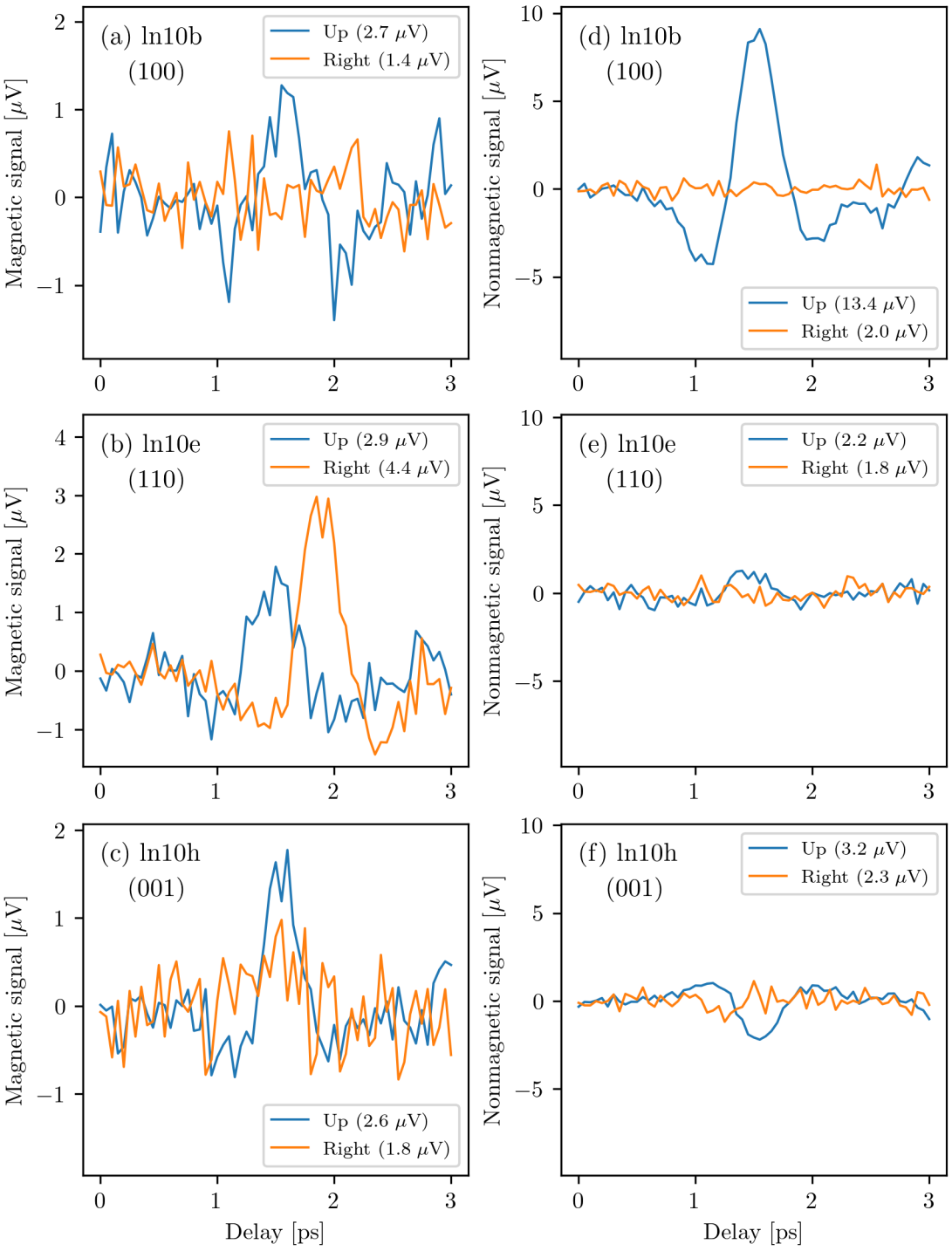

Figure 3.9: Magnetic and nonmagnetic signals from the RuO_2 samples containing a CoFeB layer. The data are taken from the previously shown measurements in the Halbach cylinder. The amplitudes of the signals are given in parentheses and the signals have been measured for two perpendicular orientations of the sample and the vertically applied magnetic field. (a) Magnetic signals from ln10b. (b) Magnetic signals from ln10e. (c) Magnetic signals from ln10h. (d) Nonmagnetic signals from ln10b. (e) Nonmagnetic signals from ln10e. (f) Nonmagnetic signals from ln10h.

3.4 RuO_2 samples with Pt layer

The samples ln10a [RuO_2 (100)/Pt], ln10d [RuO_2 (110)/Pt] and ln10g [RuO_2 (001)/Pt] were field cooled by dr. Olejník to make the magnetic structure of the RuO_2 layer uniform. We measured emission from the samples before the field cooling and after for two perpendicular orientations of the sample. Results of these measurements are shown in graphs in Figures 3.10, 3.11 and 3.12. Due to the laboratory time constraints, some measurements could not be performed for extended acquisition times and subsequently had high noise levels.

We detected signals above the noise level for samples ln10a and ln10d and perhaps a small one for ln10g which was present only before the field cooling (panels (a)) and not after it (panels (b)). The signals were present only for the vertical orientation of the sample. A possible interpretation would be that the emitted THz wave is linearly polarised and the emission is associated with the orientation of the RuO_2 crystal. The small signal from ln10g (panel (a) in Fig. 3.12) was measured only once and even though it looks very much like a wave, we cannot be certain. The measurement was averaged out of 350 loops, and it was not replicated. The measurement after field cooling was much more precise with 1340 loops so we might interpret it as a random fluctuation.

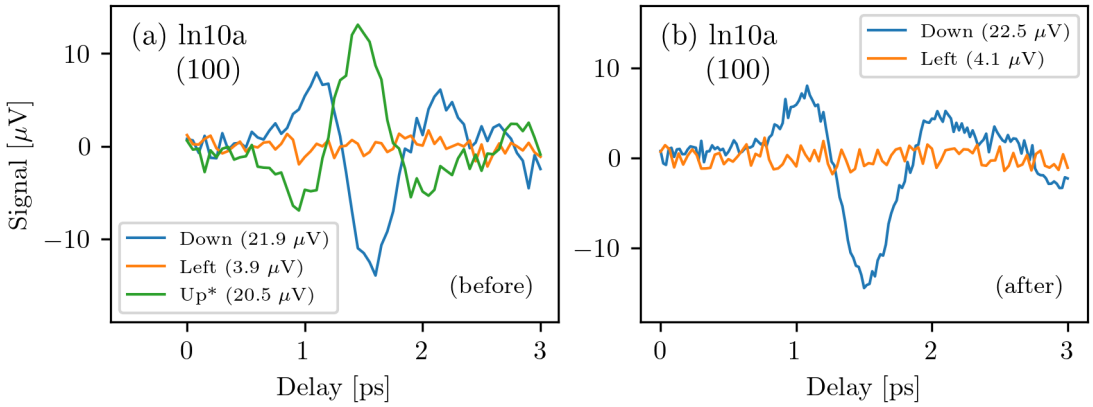

Figure 3.10: Graphs of measured signals from sample ln10a [RuO_2 (100)/Pt] for two perpendicular sample orientations. Numbers in parentheses indicate the amplitude of the measured signal. (a) Measurements of emission before field cooling the sample. The loops averaged for measurements were: 350 (left), 218 (down), and 148 (up). For the "Up*" measurement, a magnetic field of 270 mT was applied. (b) Measurements of emission after field cooling the sample. The loops averaged for measurements were: 385 (down) and 350 (left).

We also tried putting the RuO_2/Pt samples in magnetic fields in hopes of altering[8] the magnetic structure of RuO_2 and its THz emission. We tried putting the sample ln10a directly on a permanent magnet; the field at the location of the sample was measured to be around 270 mT, see Fig. 3.10. In graph 3.13, we show the results of THz emission measurements from the sample ln10d which was put inside the Halbach cylinder in up orientation and we rotated the cylinder so the magnetic field (200 mT) was applied in different directions.

[8] i. e. slightly changing directions of the anti-parallel magnetic moments of Ru atoms.

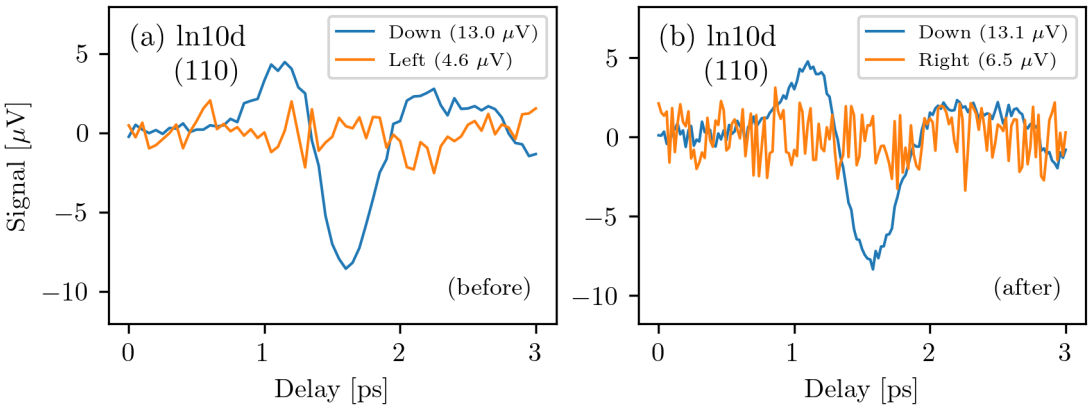

Figure 3.11: Graphs of measured signals from sample ln10d [RuO_2 (110)/Pt] for two perpendicular sample orientations. Numbers in parentheses indicate the amplitude of the measured signal. (a) Measurements of emission before field cooling the sample. The loops averaged for measurements were: 2000 (down) and 200 (left). (b) Measurements of emission after field cooling the sample. The loops averaged for measurements were: 1138 (down) and 83 (right).

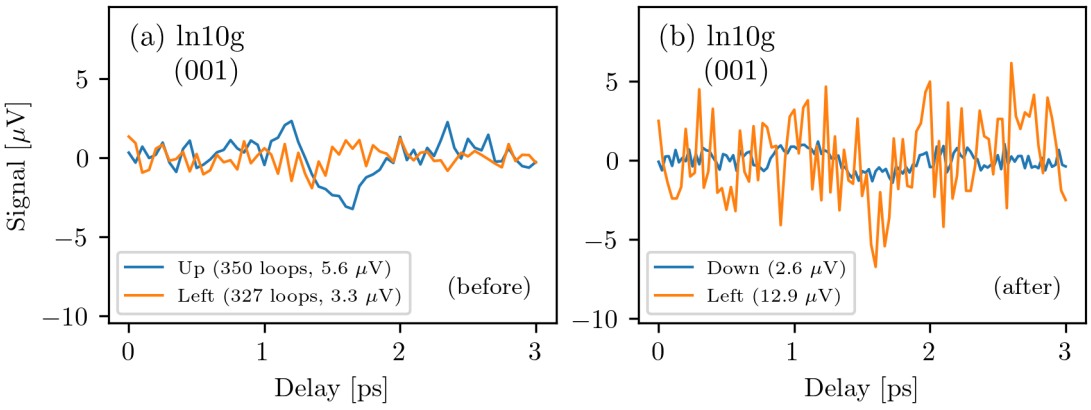

Figure 3.12: Graphs of measured signals from sample ln10g [RuO_2 (001)/Pt] for two perpendicular sample orientations. Numbers in parentheses indicate the amplitude of the measured signal. (a) Measurements of emission before field cooling the sample. The loops averaged for measurements were: 350 (up) and 327 (left). (b) Measurements of emission after field cooling the sample. The loops averaged for measurements were: 1340 (down) and 50 (left).

In the case of ln10a (Fig. 3.10), applying the magnetic field seems to change the amplitude of the measured signal (slightly – 0.6 μV increase). However, a substantial noise is present in the waveform measured (standard deviation for the first 10 points of the curve for the up orientation in panel (a) is $\approx$ 1 μV) and also we have moved the sample to put it directly on the permanent magnet so the measurement conditions were different. For these reasons, the measured change after applying the magnetic field is most likely not the result of applying a magnetic field. The measured waveforms from the sample ln10d (Fig. 3.13) also show a difference in the amplitudes measured for different magnetic field orientations. Again, it is important to note that the noise is present, and for that reason, the changes in amplitude are probably resulting from random fluctuations. We can also see that the waveform seems to have shifted in the horizontal direction—the delay of peaks of measured signals for different orientations changed. The measurements were made in the following order: up, right, down and left (the direction of the magnetic field applied). After examining the data in a different manner, i.e. making partial averages of each 100 loops in the sequence, the change of peak position seems to have been gradual in time. Thus, the cause for this change was probably a result of changes in the experimental setup in time over which we had no control.

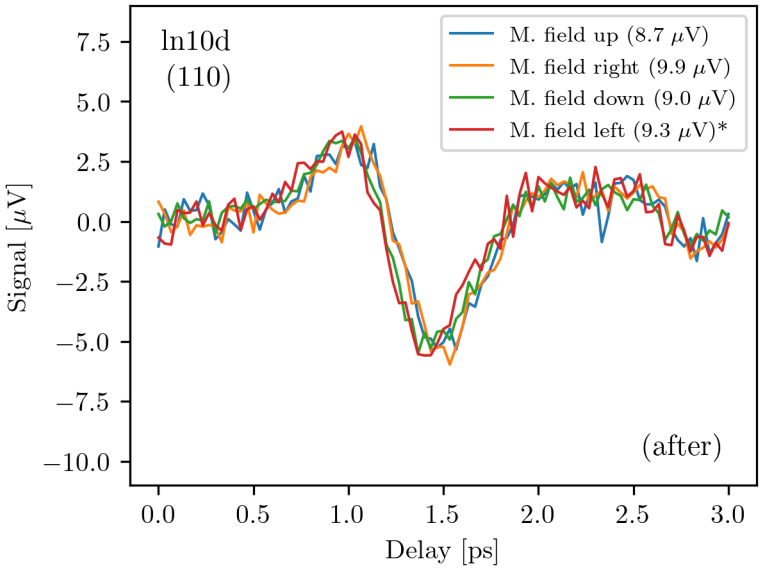

Figure 3.13: Graph of measured signals from the sample ln10d in Halbach cylinder after being field cooled and for different orientations of the magnetic field inside the cylinder. The sample was oriented up in the cylinder, and the magnetic field was rotated. Emission for four different orientations of the magnetic field was measured. The plotted waveforms are averaged from 600 loops in the case of up, right and down orientations of the field and from 338 loops for the left orientation of the field. In parentheses, amplitudes of the measured signals are given.

4. Summary and discussion

We summarise the results of the measurements presented in the sections above in tables 4.1 and 4.2. The first observation from the spectroscopic measurements is that the emission is nowhere near as strong for samples containing RuO_2 as for the reference sample ln10c (CoFeB/Pt); the amplitude of the signals is three orders of magnitude lower. Nevertheless, we detected THz radiation from the samples ln10b and ln10d, from which the THz radiation was expected to be the result of effects connected to the altermagnetic structure of RuO_2. Moreover, in all the cases, the signals were dependent on crystal rotation and, in the case of the RuO_2/CoFeB samples, on the magnetic field (thus, probably of magnetic origin).

4.1 RuO_2 samples with CoFeB layer

Table 4.1: Summary of findings from THz spectroscopy measurements on RuO_2/CoFeB samples [ln10b (100), ln10e (010), ln10h (100)]. We give intervals or upper limits of the amplitude of measured signals for the vertical orientation of the sample S^V and for horizontal orientation S^H. In the next two columns, amplitudes of magnetic signals are given for the two spatial orientations of the sample (S^V_{mag}, S^H_{mag}). The word "noise" in parentheses indicates that the highest amplitude measured was on the same level as the noise in the signal. The last column "Change?" indicates whether there was a difference between measurements with the lower magnetic field applied (10 mT) and higher magnetic field applied (200 mT). The question mark in the first row expresses that we did not make enough measurements to be certain[1].

Sample	S^V [μV]	S^H [μV]	S^V_{mag} [μV]	S^H_{mag} [μV]	Change?
ln10b	12.0 - 17.4	$<$ 2.3 (noise)	2.7	1.4 (noise)	?
ln10e	2.3 - 4.8	1.3 - 5.6	2.9	4.4	Yes
ln10h	1.9 - 5.7	$<$ 3.3 (noise)	2.6	1.8 (noise)	Yes

The measurements show a nonmagnetic signal for ln10b (Fig. 3.9, panel (d)) and comparable magnetic signals for all samples in the vertical orientation of the crystal (Fig. 3.9, panels (a)–(c)). A greater magnetic signal has been detected for horizontally oriented sample ln10e (panel (c) in Fig. 3.9), which is delayed from the other detected signals by $\sim$ 0.5 ps. For nonmagnetic signals, we also observe low signals for samples ln10e and ln10h (Fig. 3.9, panels (e), (f)), albeit 4-6$\times$ lower than for ln10b.

A process taking place in the ferromagnetic layer which is to be expected is ultrafast demagnetisation (shortly UDM) [17]. This process occurs when electrons in the ferromagnetic layers are excited by ultrashort laser pulses, followed by an ultrafast decrease of the magnetic moment of the layer. After

[1] To compare the measurements reliably, a higher precision for the measurements in the lower magnetic field and measurements with both polarities of the applied field would be necessary.

this reduction, which typically occurs within tens or hundreds of femtoseconds, a picoseconds-long relaxation back to the equilibrium value takes place. Since this process happens on a picosecond time scale (exactly the same as the one on which charge current oscillates in an STE, ref. [17]) and THz radiation is emitted from the oscillating magnetic dipole.

We can attempt a rough estimate of the expected amplitude of the signal from UDM. In ref. [17], the signal from STE corresponding to UDM is about 0.5% of the total THz emission from STE. For the signal from the reference sample ln10c (CoFeB/Pt, Fig. 3.4), this would imply that $\sim$ 24 μV of the amplitude corresponds to UDM. In the section about STEs, we show that the electric field of the THz wave is linearly dependent on the total impedance of the nonmagnetic and magnetic layers (see Eq. 2.1 and eq. (A2) in ref. [17]). To estimate how much signal would correspond to UDM in RuO_2 samples, we may try to calculate the ratio of the impedance of Pt/CoFeB layers Z_{Pt} and of RuO_2/CoFeB layers $Z_{\mathrm{RuO_2}}$. The impedance of the layer is given by the following equation [18, 29]:

$$Z(\omega) = \frac{Z_0}{n_{\mathrm{TiO_2}} + n_0 + Z_0 \int_0^d \sigma(z)\ \mathrm{d}z}, \tag{4.1}$$

where $Z_0 \approx 377\ \Omega$ is the impedance of the free space, $n_{\mathrm{TiO_2}} \approx 6$ the refractive index of the substrate TiO_2 (from ref. [30][2]), $n_0 \approx 1$ the refractive of the free space, σ the conductivity of the thin films and we integrate over the thickness d of the bilayer. We will simplify the integral to:

$$\int_0^d \sigma(z)\ \mathrm{d}z \approx \sigma_{\mathrm{FM}} d_{\mathrm{FM}} + \sigma_{\mathrm{NM}} d_{\mathrm{NM}}, \tag{4.2}$$

where we assume homogenous conductivity in the ferromagnetic layer σ_{FM} and in the nonmagnetic layer σ_{NM} with respective thicknesses d_{FM} and d_{NM}. Now we will approximately calculate the ratio of the CoFeB/Pt sample impedance and the CoFeB/RuO_2 impedance:

$$\frac{Z_{\mathrm{RuO_2}}}{Z_{\mathrm{Pt}}} \approx \frac{n_{\mathrm{TiO_2}} + n_0 + Z_0(\sigma_{\mathrm{CoFeB}} d_{\mathrm{CoFeB}} + \sigma_{\mathrm{Pt}} d_{\mathrm{Pt}})}{n_{\mathrm{TiO_2}} + n_0 + Z_0(\sigma_{\mathrm{CoFeB}} d_{\mathrm{CoFeB}} + \sigma_{\mathrm{RuO_2}} d_{\mathrm{RuO_2}})} \approx 0.4 \tag{4.3}$$

We used values $d_{\mathrm{CoFeB}} = d_{\mathrm{Pt}} = 3$ nm, $d_{\mathrm{RuO_2}} = 18$ nm and for the conductivities, $\sigma_{\mathrm{CoFeB}} \doteq 1 \approx 10^6$ S/m (from supplementary material for article [17]), $\sigma_{\mathrm{Pt}} \doteq 1 \approx 10^6$ S/m (from ref. [32]) and $\sigma_{\mathrm{RuO_2}} \approx 2 \cdot 10^6$ S/m (from resistivity measurements in ref. [20]). By this estimation, the signal from UDM should have approximately an amplitude of 10 μV. The RuO_2/CoFeB samples had ten times lower magnetisation, thus, we might estimate that the expected UDM signal should also be ten times lower. This gives us a prediction of $\sim$ 1 μV for the amplitude of the UDM signal in RuO_2/CoFeB. The magnetic signal from RuO_2/CoFeB samples in the vertical orientation had an amplitude of approximately 2.7 μV. It has similar order of magnitude, but our reasoning led us to a lower value. For the discussion of the signals, we can follow two routes:

[2]This source cites [31] as the source of the refractive index data. The last measurement given is for wavelength 125.12 μm which corresponds to about 2.4 THz, the lowest frequency in the data. Our measured THz signals have a period of about 1 ps which corresponds to a frequency of 1 THz. We assume that the dependence of TiO_2 refractive index on frequency does not change dramatically for lower THz frequencies.

(i) We can try to reason that the detected signal was from UDM. It is a signal that should be present for any optically excited ferromagnetic layer [17, 33] and we are only uncertain in its amplitude. The main argument against the interpretation of the signals, as resulting from UDM, is that we observe no magnetic signal when the crystal is rotated while the applied magnetic field remained the same. A possible explanation would be that the CoFeB layer does not have homogenous thickness across the surface of the bilayer and the ten times lower magnetic moment of the samples corresponds to that. Possibly, the parts where the CoFeB would be very thin could be coupled to the RuO_2 so strongly that magnetic moments of atoms in these parts do not change with an applied magnetic field. Perhaps, then, this relation between the layers would imply that the magnetisation of the CoFeB bilayer is highly dependent on the orientation of the RuO_2 crystal. This would explain why we do not detect the UDM signal in the horizontal orientation of the crystal—the THz wave (supposedly from UDM) is vertically polarised and our EOS detection is only sensitive to the horizontal component.

On the other hand, we observed magnetic signals, which indicates that we were able to change the magnetisation albeit part of it. Even for the horizontally oriented sample, a similar part of the magnetisation should be aligned with the vertically applied magnetic field. The SQUID measurements support this claim as the applied magnetic fields for inverting the magnetic moments of the samples were about ten times lower than in the Hallbach cylinder.

(ii) The signals can be related to the altermagnetic structure. All the signals change with the rotation of the crystal, independent of the magnetic field, suggesting a strong relationship between the THz emission and the RuO_2 crystal orientation. The signal from UDM might be too small to be measured. In such case, we cannot discern if it is present in all the measurements. The main argument against the interpretation of the signals measured, as arising from the altermagnetic order, is the observed magnetic signal for the (001) orientation. In our understanding of the magnetic structure of RuO_2, the band structure for electrons flowing from the ferromagnetic layer should be spin-independent thus, no obvious transversal current should be present. Concievably, the situation in the RuO_2 is more complex than we imagined and considered in the first two sections.

The shifted magnetic signal for ln10e (Fig. 3.9, panel (b)) in horizontal orientation is peculiar. It almost seems that it is shifted by a half period of the THz wave relative to the other THz waves detected. This would be hardly explainable by a change in the refractive index of TiO_2 by rotating the sample—the laser pulse travels through a 0.5 mm layer of TiO_2 with refractive index $n_{TiO_2} \approx 2.7$ (ref. [34] for 1030 nm wavelengths) in approximately 0.6 ps. Delaying it by changing the refraction index amounts to almost doubling the refractive index, which is an absolutely unreasonable change for a material not known for its ultra-high birefringent properties [35]. Thus, we can speculate whether it is another signal with an origin in altermagnetic effects which are not recognised at this time.

The nonmagnetic signals are also complicated to interpret. We can assume they are connected to the crystalline structure because the signal is absent for horizontal orientations of the samples. We could hypothesize that we would detect

a similar signal if our detection were sensitive to vertically polarised THz waves.

4.2 RuO_2 samples with Pt layer

Table 4.2: Summary of findings from THz spectroscopy measurements on RuO_2/Pt samples [ln10a (100), ln10d (010), ln10g (001)]. We give intervals or approximate values of the amplitude of measured signals for the vertical orientation of the sample S^V and for horizontal orientation S^H. In the last column, we write whether or not the measurements show any change after field cooling the samples. Asterisk in the last row marks a value that has not been confirmed, specifically, the measured signal from ln10g before it was field cooled where it seemed there was a THz wave present. However, it could still be attributed to noise.

Sample	S^V [μV]	S^H [μV]	Change after field cooling?
ln10a	~ 22	3.9 - 4.1 (noise)	No
ln10d	~ 13	4.6 - 6.5 (noise)	No
ln10g	2.6 or 5.6*	3.3 - 12.9 (noise)	?

For RuO_2/Pt samples, THz radiation was detected for vertically oriented ln10a, ln10d and perhaps for ln10g before it was field cooled (Figures 3.10–3.12). However, the amplitude of THz radiation from ln10g was close to the level of noise (the standard deviation for the first 10 points of the curve for the up orientation before the field cooling is ≈ 0.6 μV). For horizontal orientations of the samples, no THz radiation has been detected. No effect of magnetic field 200 mT on the emission from sample ln10d has been observed.

Processes responsible for the emission of THz radiation remain obscure. We could attribute the emission from ln10d to the spin-polarised current from RuO_2, which we expected, but a greater signal from ln10a was measured, which was not predicted. As mentioned above, the processes in RuO_2 might differ from our theories. The emission seems to be connected to the crystal orientation. We can speculate that the reason why we do not observe THz signals for the horizontal orientations is that the THz wave is polarised vertically, thus, our EOS detection cannot detect it.

A fact that goes against the assumption that the signals are of altermagnetic origin is that the samples did not show much change after field cooling. After the growth, the magnetic order of RuO_2 was probably inhomogenous—the parts of the altermagnet had the magnetic moments antiparallel but these microscopic parts did not all have the same relative orientation. After the field cooling, there is a much bigger chance that the RuO_2 layer was relatively homogenous. In such case, we would expect the signals connected with the altermagnetic order to increase in amplitude.

4.3 Future experiments

We could pursue the idea of studying RuO_2 in STEs in future experiments and use the knowledge acquired by our measurements. The manufacturing of the samples could be refined. The CoFeB magnetic layer with the much lower magnetic moment results in a problematic analysis of the origin of the signals. If a thicker ferromagnetic layer was grown, the magnetic moments of the reference sample and the other ferromagnet-altermagnet samples would possibly be comparable. Also, the UDM signal could be greater. Another factor which could be changed is the choice of ferromagnetic material. Material with a simpler crystalline structure, like Fe, could be used, which would simplify the analysis of processes in the STE.

Growing the RuO_2 on a different substrate than TiO_2, which would be transparent for THz radiation, could be promising. However, TiO_2 is hardly replaceable because of the shared crystal lattice type and similar lattice constants and achieving epitaxial growth for another substrate material could be problematic.

Platinum as the nonmagnetic metal layer is ideal for its high spin Hall angle, although it would be of interest to also grow RuO_2 bilayers with wolfram because it has a negative spin Hall angle [12].

The CoFeB and Pt layers were grown on the RuO_2 by a different manufacturer than the RuO_2 on TiO_2. The interface quality might improve if both altermagnetic and ferromagnetic/nonmagnetic layers were grown by one manufacturer, preferably *in situ*. The interface quality in STEs is a very important factor, as are the thicknesses of the layers [29]. A thinner RuO_2 layer could also be beneficial as the resulting bilayer would have higher impedance and would also absorb less THz radiation.

An experiment to consider with the current samples could be rotating the EOS detection to detect THz waves polarised in the vertical direction. We could repeat the measurements where we detected a signal and see if the polarisation rotated with the crystal or not.

Another issue for the experiments was the time requirements of the measurements due to noise and the resulting need for longer averaging. The measurements were carried out under ordinary room temperature, atmospheric pressure and humidity. The humidity poses a problem because of the reflections of emitted THz waves on water vapours. If the experiments were done with the THz waves propagating through dry air, possibly, less noise would be present.

Conclusion

Our experiments did not provide a straightforward insight into the mechanisms of altermagnetic materials. Yet, the results are not easily explained by known processes and the signals did change with the rotation of the RuO_2 crystal, hinting at unknown effects connected to the altermagnetic structure. The measurement results indicate that the physical phenomena in altermagnets may be excitingly rich. Studying these phenomena with spintronic terahertz emitters proves to be challenging in different aspects. In the discussion, we provided suggestions for overcoming some of the challenges. Hopefully, we will soon gain a better understanding of altermagnetic materials as they possess an intriguing potential for future spintronics applications.

Bibliography

1. ŠMEJKAL, Libor; SINOVA, Jairo; JUNGWIRTH, Tomas. Emerging Research Landscape of Altermagnetism. *Physical Review X* [online]. 2022, vol. 12, no. 4 [visited on 2023-02-15]. ISSN 2160-3308. Available from DOI: 10.1103/PhysRevX.12.040501.
2. ŽUTIĆ, Igor; FABIAN, Jaroslav; SARMA, S. Das. Spintronics: Fundamentals and applications. *Reviews of Modern Physics* [online]. 2004, vol. 76, no. 2, pp. 323–410 [visited on 2023-04-21]. ISSN 0034-6861. Available from DOI: 10.1103/RevModPhys.76.323.
3. JUNGWIRTH, T.; MARTI, X.; WADLEY, P.; WUNDERLICH, J. Antiferromagnetic spintronics. *Nature Nanotechnology* [online]. 2016, vol. 11, no. 3, pp. 231–241 [visited on 2023-02-16]. ISSN 1748-3387. Available from DOI: 10.1038/nnano.2016.18.
4. SEIFERT, T.; JAISWAL, S.; MARTENS, U.; HANNEGAN, J.; BRAUN, L.; MALDONADO, P.; FREIMUTH, F.; KRONENBERG, A.; HENRIZI, J.; RADU, I.; BEAUREPAIRE, E.; MOKROUSOV, Y.; OPPENEER, P. M.; JOURDAN, M.; JAKOB, G.; TURCHINOVICH, D.; HAYDEN, L. M.; WOLF, M.; MÜNZENBERG, M.; KLÄUI, M.; KAMPFRATH, T. Efficient metallic spintronic emitters of ultrabroadband terahertz radiation. *Nature Photonics* [online]. 2016, vol. 10, no. 7, pp. 483–488 [visited on 2023-02-15]. ISSN 1749-4885. Available from DOI: 10.1038/nphoton.2016.91.
5. BAI, H.; HAN, L.; FENG, X. Y.; ZHOU, Y. J.; SU, R. X.; WANG, Q.; LIAO, L. Y.; ZHU, W. X.; CHEN, X. Z.; PAN, F.; FAN, X. L.; SONG, C. Observation of Spin Splitting Torque in a Collinear Antiferromagnet RuO 2. *Physical Review Letters* [online]. 2022, vol. 128, no. 19 [visited on 2023-02-17]. ISSN 0031-9007. Available from DOI: 10.1103/PhysRevLett.128.197202.
6. GONZÁLEZ-HERNÁNDEZ, Rafael; ŠMEJKAL, Libor; VÝBORNÝ, Karel; YAHAGI, Yuta; SINOVA, Jairo; JUNGWIRTH, Tomáš; ŽELEZNÝ, Jakub. Efficient Electrical Spin Splitter Based on Nonrelativistic Collinear Antiferromagnetism. *Physical Review Letters* [online]. 2021, vol. 126, no. 12 [visited on 2023-02-16]. ISSN 0031-9007. Available from DOI: 10.1103/PhysRevLett.126.127701.
7. MAEKAWA, Sadamichi; VALENZUELA, Sergio O.; SAITOH, Eiji; KIMURA, Takashi. *Spin Current*. Oxford University Press, 2017. ISBN 9780198787075. Available from DOI: 10.1093/oso/9780198787075.001.0001.
8. COEY, J. M. D. *Magnetism and Magnetic Materials*. 4th printing. Cambridge: Cambridge University Press, 2010. ISBN 9780521016766. Available from DOI: 10.1017/CBO9780511845000.
9. SAKURAI, J. J.; NAPOLITANO, Jim. *Modern Quantum Mechanics* [online]. Third. Cambridge: Cambridge University Press, 2020-10-10 [visited on 2023-03-16]. ISBN 9781108587280. Available from DOI: 10.1017/9781108587280.

10. MAEKAWA, Sadamichi; KIKKAWA, Takashi; CHUDO, Hiroyuki; IEDA, Jun'ichi; SAITOH, Eiji. Spin and spin current—From fundamentals to recent progress. *Journal of Applied Physics* [online]. 2023-01-14, vol. 133, no. 2, pp. 020902-1 - 020902–24 [visited on 2023-03-14]. ISSN 0021-8979. Available from DOI: 10.1063/5.0133335.

11. WU, M.W.; JIANG, J.H.; WENG, M.Q. Spin dynamics in semiconductors. *Physics Reports* [online]. 2010, vol. 493, no. 2-4, pp. 61–236 [visited on 2023-04-21]. ISSN 03701573. Available from DOI: 10.1016/j.physrep.2010.04.002.

12. SINOVA, Jairo; VALENZUELA, Sergio O.; WUNDERLICH, J.; BACK, C. H.; JUNGWIRTH, T. Spin Hall effects. *Reviews of Modern Physics* [online]. 2015, vol. 87, no. 4, pp. 1213–1260 [visited on 2023-03-16]. ISSN 0034-6861. Available from DOI: 10.1103/RevModPhys.87.1213.

13. MATTIS, Daniel Charles. *The theory of magnetism made simple: An introduction to physical concepts and to some useful mathematical methods*. Singapore: World Scientific, 2006. ISBN 978-981-3102-22-4. Available from DOI: 10.1142/5372.

14. BLUNDELL, Stephen. *Magnetism in condensed matter*. 1st edition. New York: Oxford University Press, 2001. ISBN 0198505922.

15. BOSE, Arnab; SCHREIBER, Nathaniel J.; JAIN, Rakshit; SHAO, Ding-Fu; NAIR, Hari P.; SUN, Jiaxin; ZHANG, Xiyue S.; MULLER, David A.; TSYMBAL, Evgeny Y.; SCHLOM, Darrell G.; RALPH, Daniel C. Tilted spin current generated by the collinear antiferromagnet ruthenium dioxide. *Nature Electronics* [online]. 2022, vol. 5, no. 5, pp. 267–274 [visited on 2023-03-21]. ISSN 2520-1131. Available from DOI: 10.1038/s41928-022-00744-8.

16. ŠMEJKAL, Libor; SINOVA, Jairo; JUNGWIRTH, Tomas. Beyond Conventional Ferromagnetism and Antiferromagnetism: A Phase with Nonrelativistic Spin and Crystal Rotation Symmetry. *Physical Review X* [online]. 2022, vol. 12, no. 3, pp. 031042-1 - 031042–16 [visited on 2023-03-17]. ISSN 2160-3308. Available from DOI: 10.1103/PhysRevX.12.031042.

17. ROUZEGAR, Reza; BRANDT, Liane; NÁDVORNÍK, Lukáš; REISS, David A.; CHEKHOV, Alexander L.; GUECKSTOCK, Oliver; IN, Chihun; WOLF, Martin; SEIFERT, Tom S.; BROUWER, Piet W.; WOLTERSDORF, Georg; KAMPFRATH, Tobias. Laser-induced terahertz spin transport in magnetic nanostructures arises from the same force as ultrafast demagnetization. *Physical Review B* [online]. 2022, vol. 106, no. 14, pp. 144427-1 - 144427–22 [visited on 2023-04-22]. ISSN 2469-9950. Available from DOI: 10.1103/PhysRevB.106.144427.

18. SEIFERT, T.; MARTENS, U.; GÜNTHER, S.; SCHOEN, M. A. W.; RADU, F.; CHEN, X. Z.; LUCAS, I.; RAMOS, R.; AGUIRRE, M. H.; ALGARABEL, P. A.; ANADÓN, A.; KÖRNER, H. S.; WALOWSKI, J.; BACK, C.; IBARRA, M. R.; MORELLÓN, L.; SAITOH, E.; WOLF, M.; SONG, C.; UCHIDA, K.; MÜNZENBERG, M.; RADU, I.; KAMPFRATH, T. Terahertz Spin Currents and Inverse Spin Hall Effect in Thin-Film Heterostructures Containing Complex Magnetic

Compounds. *SPIN* [online]. 2017-10-10, vol. 07, no. 03, pp. 1740010-01 - 1740010–11 [visited on 2023-03-12]. ISSN 2010-3247. Available from DOI: 10.1142/S2010324717400100.

19. BERLIJN, T.; SNIJDERS, P. C.; DELAIRE, O.; ZHOU, H.-D.; MAIER, T. A.; CAO, H.-B.; CHI, S.-X.; MATSUDA, M.; WANG, Y.; KOEHLER, M. R.; KENT, P. R. C.; WEITERING, H. H. Itinerant Antiferromagnetism in RuO 2. *Physical Review Letters* [online]. 2017, vol. 118, no. 7, pp. 077201-1 - 077201–6 [visited on 2023-03-21]. ISSN 0031-9007. Available from DOI: 10.1103/PhysRevLett.118.077201.

20. FENG, Zexin; ZHOU, Xiaorong; ŠMEJKAL, Libor; WU, Lei; ZHU, Zengwei; GUO, Huixin; GONZÁLEZ-HERNÁNDEZ, Rafael; WANG, Xiaoning; YAN, Han; QIN, Peixin; ZHANG, Xin; WU, Haojiang; CHEN, Hongyu; MENG, Ziang; LIU, Li; XIA, Zhengcai; SINOVA, Jairo; JUNGWIRTH, Tomáš; LIU, Zhiqi. An anomalous Hall effect in altermagnetic ruthenium dioxide. *Nature Electronics* [online]. 2022, vol. 5, no. 11, pp. 735–743 [visited on 2023-04-23]. ISSN 2520-1131. Available from DOI: 10.1038/s41928-022-00866-z.

21. DEXHEIMER, Susan L. *Terahertz Spectroscopy: Principles and Applications* [online]. 1st ed. Boca Raton: CRC Press, 2008 [visited on 2021-10-12]. ISBN 9781315221762. Available from: https://doi.org/10.1201/9781420007701.

22. HECHT, Eugene. *Optics*. Fifth edition, global edition. Boston: Pearson Education Limited, [2017]. ISBN 978-1-292-09693-3.

23. RIEK, C.; SELETSKIY, D. V.; MOSKALENKO, A. S.; SCHMIDT, J. F.; KRAUSPE, P.; ECKART, S.; EGGERT, S.; BURKARD, G.; LEITENSTORFER, A. Direct sampling of electric-field vacuum fluctuations. *Science* [online]. 2015-10-23, vol. 350, no. 6259, pp. 420–423 [visited on 2023-03-20]. ISSN 0036-8075. Available from DOI: 10.1126/science.aac9788.

24. VOSS, R.F. 1/f (Flicker) Noise: A Brief Review. In: *33rd Annual Symposium on Frequency Control* [online]. Atlantic City, NJ, USA: IEEE, 1979, pp. 40–46 [visited on 2023-04-17]. Available from DOI: 10.1109/FREQ.1979.200297.

25. SHEPELIN, Nick A.; TEHRANI, Zahra P.; OHANNESSIAN, Natacha; SCHNEIDER, Christof W.; PERGOLESI, Daniele; LIPPERT, Thomas. A practical guide to pulsed laser deposition. *Chemical Society Reviews* [online]. 2023, pp. 1–28 [visited on 2023-03-23]. ISSN 0306-0012. Available from DOI: 10.1039/D2CS00938B.

26. GHAZAL, Humaira; SOHAIL, Nadeem. Sputtering Deposition. In: YANG, Dr. Dongfang (ed.). *Thin Films - Deposition Methods and Applications*. Rijeka: IntechOpen, 2022, chap. 2. Available from DOI: 10.5772/intechopen.107353.

27. TINKHAM, Michael. *Introduction to superconductivity*. Second Edition. New York: McGraw-Hill, 1996. ISBN 0-07-064878-6.

28. HALBACH, Klaus. Strong Rare Earth Cobalt Quadrupoles. *IEEE Transactions on Nuclear Science* [online]. 1979, vol. 26, no. 3, pp. 3882–3884 [visited on 2023-04-23]. ISSN 0018-9499. Available from DOI: 10.1109/TNS.1979.4330638.

29. JECHUMTÁL, Jiří. *Studium terahertzového záření emitovaného pomocí spintronických jevů*. Prague, 2020. Bachelor's thesis. Univerzita Karlova.

30. POLYANSKIY, Mikhail N. *Refractive index database* [online]. [visited on 2023-04-26]. Available from: https://refractiveindex.info.

31. SIEFKE, Thomas; KROKER, Stefanie; PFEIFFER, Kristin; PUFFKY, Oliver; DIETRICH, Kay; FRANTA, Daniel; OHLÍDAL, Ivan; SZEGHALMI, Adriana; KLEY, Ernst-Bernhard; TÜNNERMANN, Andreas. Materials Pushing the Application Limits of Wire Grid Polarizers further into the Deep Ultraviolet Spectral Range. *Advanced Optical Materials* [online]. 2016, vol. 4, no. 11, pp. 1780–1786 [visited on 2023-04-26]. ISSN 2195-1071. Available from DOI: 10.1002/adom.201600250.

32. KIM, Hyo Jin K.; KAPLAN, Kirsten E.; SCHINDLER, Peter; XU, Shicheng; WINTERKORN, Martin M.; HEINZ, David B.; ENGLISH, Timothy S.; PROVINE, J.; PRINZ, Fritz B.; KENNY, Thomas W. Electrical Properties of Ultrathin Platinum Films by Plasma-Enhanced Atomic Layer Deposition. *ACS Applied Materials & Interfaces* [online]. 2019-03-06, vol. 11, no. 9, pp. 9594–9599 [visited on 2023-04-24]. ISSN 1944-8244. Available from DOI: 10.1021/acsami.8b21054.

33. ZHANG, Wentao; MALDONADO, Pablo; JIN, Zuanming; SEIFERT, Tom S.; ARABSKI, Jacek; SCHMERBER, Guy; BEAUREPAIRE, Eric; BONN, Mischa; KAMPFRATH, Tobias; OPPENEER, Peter M.; TURCHINOVICH, Dmitry. Ultrafast terahertz magnetometry. *Nature Communications* [online]. 2020, vol. 11, no. 1, pp. 1–9 [visited on 2023-04-24]. ISSN 2041-1723. Available from DOI: 10.1038/s41467-020-17935-6.

34. DEVORE, J. R. Refractive Indices of Rutile and Sphalerite. *Journal of the Optical Society of America* [online]. 1951, vol. 41, no. 6, pp. 416–419 [visited on 2023-04-26]. ISSN 0030-3941. Available from DOI: 10.1364/JOSA.41.000416.

35. SEGURA, A.; ARTÚS, L.; CUSCÓ, R.; TANIGUCHI, T.; CASSABOIS, G.; GIL, B. Natural optical anisotropy of h-BN: Highest giant birefringence in a bulk crystal through the mid-infrared to ultraviolet range. *Physical Review Materials* [online]. 2018, vol. 2, no. 2, pp. 024001-1 - 024001–6 [visited on 2023-04-24]. ISSN 2475-9953. Available from DOI: 10.1103/PhysRevMaterials.2.024001.

List of Figures

1.1 Schematical illustration of spin Hall effects 6
1.2 Illustration of hysteresis and exchange bias 8
1.3 Illustration of altermagnet sublattice symmetry relations and spin-split band structure 9
1.4 Collinear magnetism - energy isocurves 9

2.1 STE illustration 11
2.2 Crystalographic structure of RuO_2 14
2.3 Spin current generation in RuO_2 14
2.4 Schematic RuO_2 electron energy Fermi surfaces with applied electric field 15
2.5 Illustration of the EOS detection dependence on the THz wave polarity 16
2.6 Electro-optic sampling detection method 17
2.7 Laboratory setup for THz wave generation and detection 18
2.8 Optimised STE THz wave graph 19
2.9 Manufactured sample illustration 21

3.1 SQUID measurement for ln10f 24
3.2 SQUID measurement for ln10b, ln10e, ln10h 24
3.3 SQUID measurements for ln10e showing exchange bias 25
3.4 Reference sample THz wave graph 26
3.5 Sample in sample holder illustration 27
3.6 THz emission of ln10e 29
3.7 THz emission of ln10h 29
3.8 THz emission of ln10b 30
3.9 Magnetic and nonmagnetic signals from the RuO_2 samples containing a CoFeB layer 32
3.10 THz emission of ln10a 33
3.11 THz emission of ln10d 34
3.12 THz emission of ln10g 34
3.13 THz emission of ln10d for different directions of the magnetic field 35